J. Fluid Mech. (2008), *vol.* 605, *pp.* 115–143.
doi:10.1017/S0022112008001407 Printed in the United Kingdom

The limiting form of inertial instability in geophysical flows

STEPHEN D. GRIFFITHS†

Department of Atmospheric Sciences, University of Washington, Seattle, WA 98195, USA

(Received 10 May 2007 and in revised form 28 February 2008)

The instability of a rotating, stratified flow with arbitrary horizontal cross-stream shear is studied, in the context of linear normal modes with along-stream wavenumber k and vertical wavenumber m. A class of solutions are developed which are highly localized in the horizontal cross-stream direction around a particular streamline. A Rayleigh–Schrödinger perturbation analysis is performed, yielding asymptotic series for the frequency and structure of these solutions in terms of k and m. The accuracy of the approximation improves as the vertical wavenumber increases, and typically also as the along-stream wavenumber decreases. This is shown to correspond to a near-inertial limit, in which the solutions are localized around the global minimum of fQ, where f is the Coriolis parameter and Q is the vertical component of the absolute vorticity. The limiting solutions are near-inertial waves or inertial instabilities, according to whether the minimum value of fQ is positive or negative.

We focus on the latter case, and investigate how the growth rate and structure of the solutions changes with m and k. Moving away from the inertial limit, we show that the growth rate always decreases, as the inertial balance is broken by a stabilizing cross-stream pressure gradient. We argue that these solutions should be described as non-symmetric inertial instabilities, even though their spatial structure is quite different to that of the symmetric inertial instabilities obtained when k is equal to zero.

We use the analytical results to predict the growth rates and phase speeds for the inertial instability of some simple shear flows. By comparing with results obtained numerically, it is shown that accurate predictions are obtained by using the first two or three terms of the perturbation expansion, even for relatively small values of the vertical wavenumber. Limiting expressions for the growth rate and phase speed are given explicitly for non-zero k, for both a hyperbolic-tangent velocity profile on an f-plane, and a uniform shear flow on an equatorial β-plane.

1. Introduction

An important problem in geophysical fluid dynamics is determining the stability of an inviscid flow with horizontal shear. Here we consider the linear stability of a steady parallel flow, arbitrarily sheared in the horizontal cross-stream direction, to three-dimensional disturbances, in the presence of background rotation and a vertical density stratification. The configuration is illustrated in figure 1. We study the relatively simple case in which the background stratification is uniform, so that the homegeneity

† Present address: Department of Physics, University of Toronto, 60 St George Street, Toronto, ON, M5S 1A7, Canada.

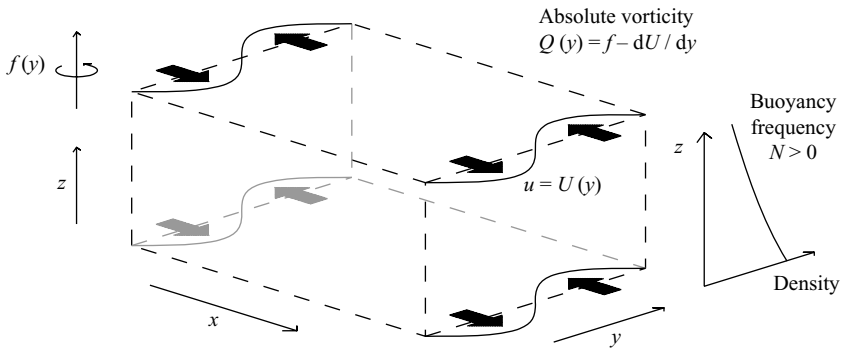

FIGURE 1. Configuration of the background flow.

in both the along-stream and vertical directions allows normal-mode disturbances with along-stream wavenumber k and vertical wavenumber m to be found. The mathematical formulation can then be reduced to a one-dimensional eigenvalue problem for the cross-stream structure and a complex frequency ω. Typically there are several families for $\omega(k, m)$, each containing a discrete or continuous spectrum of eigenvalues, corresponding to diverse motions such as Rossby waves and inertia–gravity waves. Despite the idealized nature of the formulation, results from this approach remain an important aid to understanding motions in the atmosphere and ocean.

When $k = 0$, the eigenvalue problem is relatively simple, being governed by a Schrödinger equation with potential function fQ, where f is the Coriolis parameter and Q is the vertical component of the absolute vorticity. Our analysis is based on the observation that solutions exist which become highly localized in the cross-stream direction as $|m| \to \infty$, on a length scale proportional to $|m|^{-1/2}$. This scale separation between disturbance and basic state proves to be enough to determine almost trivially the first two terms of asymptotic series for the disturbance structure and ω, using a Rayleigh–Schrödinger perturbation analysis. These solutions, which we refer to as symmetric, describe an inertial limit: that is, solutions for which the horizontal pressure gradient terms are negligible. Although this kind of mathematical reduction has been exploited for unstratified flows (Bayly 1988; Leblanc & Cambon 1997; Sipp & Jacquin 2000), it seems to have attracted only sporadic attention for stratified flows (e.g. Llewellyn Smith 1999, Appendix B). However, it simply corresponds to the scenario described by a well-known heuristic 'pressureless' parcel argument (e.g. Holton 1992). We obtain near-inertial waves when $fQ > 0$ everywhere, which are well studied in the context of upper ocean dynamics, often at small Rossby number (e.g. Kunze 1985). In contrast, when $fQ < 0$ somewhere in the flow (which requires Rossby numbers of order unity), we obtain inertial instabilities, which are often referred to as centrifugal instabilities. Whilst sufficiently strong shears could lead to such instabilities in the extratropics (e.g. Potylitsin & Peltier 1998; Shen & Evans 2002), they are more likely to occur near the equator, where they are active in both the atmosphere (e.g. Hayashi, Shiotani & Gille 1998; Knox 2003 and references therein) and ocean (e.g. Richards & Edwards 2003; d'Orgeville *et al.* 2004).

When $k \neq 0$, the complexity of the eigenvalue problem means that little can be said analytically about the stability of an arbitrary shear flow to fully three-dimensional disturbances. This reflects an underlying physical complexity, since as k and m vary across all possible values, we encounter solutions ranging from barotropic instabilities

(or Rossby waves) with vertical structure, to inertial instabilities (or inertia–gravity waves) with along-stream structure. Classification of such solutions can be difficult (e.g. Taniguchi & Ishiwatari 2006). Any simplification to the mathematics, or to the underlying physics, is desirable. Here we show how a Rayleigh–Schrödinger perturbation analysis can be applied when $k \neq 0$, again almost trivially leading to solutions localized upon a length scale $\propto |m|^{-1/2}$ as $|m| \to \infty$. These $k \neq 0$ solutions, which we refer to as non-symmetric, smoothly connect to the symmetric near-inertial solutions obtained as $k \to 0$ and $|m| \to \infty$, and can thus be unambiguously described as their extension to finite k. We shall focus on flows for which $fQ < 0$ somewhere, in which case the solutions are non-symmetric inertial instabilities. This approach has been used by Clark & Haynes (1996) to examine the instability of a uniform shear flow on the equatorial β-plane, but here we extend it to quite arbitrary shear flows and background rotation. There are no *a priori* restrictions on k, and few on the cross-stream shear of the basic flow, so we are able to investigate fully the effects of along-stream asymmetries and non-uniform shear. The results obtained are similar in nature to those of Billant & Gallaire (2005), who used a WKB analysis to examine the stability of flows with circular symmetry.

Our approach is as follows. After specifying the governing equations, we introduce the asymptotic method in § 2, where it is applied to the relatively simple case of symmetric solutions ($k = 0$). The main results are expressions for the frequency and cross-stream structure of the solutions as power series in $|m|^{-1}$, valid as $|m| \to \infty$. The approach is generalized to non-symmetric solutions ($k \neq 0$) in § 3. We then make two detailed comparisons of the theory with numerically determined solutions: the instability of a hyperbolic-tangent velocity profile on an f-plane, in § 4, and the instability of a uniform shear flow on an equatorial β-plane, in § 5. The results are discussed in § 6.

1.1. *The governing equations*

Using a set of Cartesian coordinates, with horizontal along-stream coordinate x and cross-stream coordinate y, and corresponding velocity components u and v, we consider a basic flow $u = U(y)$ (see figure 1). We suppose that the fluid has constant buoyancy frequency N, and that the hydrostatic and traditional approximations are valid (some comments regarding other cases are given in § 6.1). Then we model the evolution of linear, normal mode disturbances to the flow with a vertical wavenumber m via

$$\mathscr{D}\tilde{u} - Q\tilde{v} = -\frac{\partial\tilde{\phi}}{\partial x}, \quad \mathscr{D}\tilde{v} + f\tilde{u} = -\frac{\partial\tilde{\phi}}{\partial y}, \quad \mathscr{D}\tilde{\phi} + \frac{N^2}{m^2}\left(\frac{\partial\tilde{u}}{\partial x} + \frac{\partial\tilde{v}}{\partial y}\right) = 0. \qquad (1.1a\text{–}c)$$

Here $\mathscr{D} = \partial/\partial t + U(y)\partial/\partial x$, the Coriolis parameter f is an arbitrary function of y, $Q(y) = f - \mathrm{d}U/\mathrm{d}y$, and the disturbances take the form

$$(\tilde{u}, \tilde{v}, \tilde{\phi}) = \mathrm{Re}\left\{(\tilde{U}(y), \tilde{V}(y), \tilde{\Phi}(y))\tilde{Z}(z)\mathrm{e}^{\mathrm{i}(kx-\omega t)}\right\}, \qquad (1.2)$$

where k is a real along-stream wavenumber. The physical interpretation of z, $\tilde{\phi}(x, y, z, t)$, and the vertical structure function $\tilde{Z}(z)$ depends upon the equations used to model the vertical structure of the fluid. With the Boussinesq equations, z is a geometrical coordinate, $\tilde{\phi}$ simply corresponds to the pressure perturbation divided by a reference density, and $\tilde{Z}(z) = \mathrm{e}^{\mathrm{i}mz}$ (e.g. Salmon 1998, § 2.16). With the primitive equations, z is a log-pressure coordinate, $\tilde{\phi}$ is the geopotential, and $\tilde{Z}(z) = \mathrm{e}^{z/2H}\mathrm{e}^{\mathrm{i}\tilde{m}z}$, where $m^2 = \tilde{m}^2 + 1/4H^2$, and H is a scale height (e.g. Andrews, Holton & Leovy 1987, § 4.7). Equations (1.1*a*)–(1.1*c*) also describe disturbances to a one-layer flow of

uniform depth h, if N^2/m^2 is replaced by gh. A more general stability analysis for one-layer flow is given by Ripa (1983).

Generally, (1.1*a–c*) can be manipulated into a single equation for $\tilde{V}(y)$:

$$\frac{\mathrm{d}^2\tilde{V}}{\mathrm{d}y^2}+\left(\frac{2k\hat{\omega}U'}{\hat{\omega}^2-N^2k^2/m^2}\right)\frac{\mathrm{d}\tilde{V}}{\mathrm{d}y}+\left(\frac{m^2}{N^2}(\hat{\omega}^2-fQ)-k^2-\frac{kQ'}{\hat{\omega}}-\frac{2k^2QU'}{\hat{\omega}^2-N^2k^2/m^2}\right)\tilde{V}=0, \tag{1.3}$$

which is equation (3.14) of Boyd (1978) for instance, where $U'=\mathrm{d}U/\mathrm{d}y$, and

$$\hat{\omega}(y)=\omega-kU(y). \tag{1.4}$$

To complete the formulation, we must specify the y-domain and appropriate boundary conditions, turning (1.3) into an eigenvalue problem for the unknown frequency ω. We consider an unbounded flow $-\infty<y<\infty$ with

$$\tilde{V}\to 0 \text{ as } |y|\to\infty. \tag{1.5}$$

However, since the solutions we develop are localized, the analysis also applies to bounded and periodic domains.

A bound on the growth rate $\mathrm{Im}(\omega)$ can be obtained by considering a disturbance energy (cf. the corresponding analysis of Yavneh, McWilliams & Molemaker (2001) for a cylindrical geometry). Substituting (1.2) into (1.1), forming $\tilde{U}^*\times(1.1a)+\tilde{V}^*\times(1.1b)+(m/N)^2\tilde{\Phi}^*\times(1.1c)$, taking the real part, integrating from $-\infty$ to ∞ and using (1.5), gives

$$\mathrm{Im}\,(\omega)=\frac{-\displaystyle\int_{-\infty}^{\infty}U'(y)\mathrm{Re}\left(\tilde{U}^*\tilde{V}\right)\,\mathrm{d}y}{\displaystyle\int_{-\infty}^{\infty}\left(|\tilde{U}|^2+|\tilde{V}|^2+(m/N)^2|\tilde{\Phi}|^2\right)\mathrm{d}y}.$$

Since $0\leqslant|\tilde{U}\pm\tilde{V}|^2=(\tilde{U}\pm\tilde{V})(\tilde{U}^*\pm\tilde{V}^*)$, which implies that $2|\mathrm{Re}(\tilde{U}\tilde{V}^*)|\leqslant|\tilde{U}|^2+|\tilde{V}|^2$,

$$|\mathrm{Im}\,\omega|\leqslant\frac{\max(|U'(y)|)\displaystyle\int_{-\infty}^{\infty}|\mathrm{Re}(\tilde{U}^*\tilde{V})|\,\mathrm{d}y}{\displaystyle\int_{-\infty}^{\infty}(|\tilde{U}|^2+|\tilde{V}|^2+(m/N)^2|\tilde{\Phi}|^2)\mathrm{d}y}\leqslant\frac{\max(|U'(y)|)}{2}. \tag{1.6}$$

2. Symmetric solutions

Symmetric solutions of (1.1*a–c*), i.e. those with $k=0$, are of two types. The first type, with $\tilde{v}=0$ and $\omega=0$, are not studied here. We consider the second type, with $\tilde{v}\neq 0$, which are obtained by setting $k=0$ in (1.3):

$$\frac{\mathrm{d}^2\tilde{V}}{\mathrm{d}y^2}+\frac{m^2}{N^2}(\omega^2-fQ)\tilde{V}=0. \tag{2.1}$$

This is a Schrödinger equation with eigenvalue ω^2. We suppose that

(i) fQ is smooth, (2.2*a*)

(ii) fQ has a unique global minimum $y=\overline{y}$, where $(fQ)''>0$, (2.2*b*)

(iii) $\min(fQ)<(fQ)_\infty$, where $(fQ)_\infty=\min\{\lim_{y\to-\infty}fQ,\lim_{y\to\infty}fQ\}$. (2.2*c*)

With (1.5), this implies the existence of a set of discrete eigenvalues (e.g. Messiah 2000, § 3.10). If $fQ\to\infty$ as $|y|\to\infty$, the discrete set is countably infinite, with $\omega^2>\min(fQ)$.

If $(fQ)_\infty$ is bounded, the discrete set is finite, with $\min(fQ) < \omega^2 < (fQ)_\infty$. In this latter case, there is also a continuous spectrum of eigenvalues with $\omega^2 > (fQ)_\infty$, but the corresponding eigensolutions do not satisfy (1.5). Such solutions are not considered here.

2.1. *The leading-order near-inertial solution*

We develop approximations for the discrete eigenvalues and eigenmodes satisfying (1.5) and (2.1). We seek solutions which are localized on a length scale L about a particular streamline $y = \overline{y}$, and thus work in terms of a transformed cross-stream coordinate

$$Y = \frac{y - \overline{y}}{L}. \tag{2.3}$$

Although not immediately obvious, (2.1) has a distinguished limit for a particular scaling of $L \to 0$ and $|m| \to \infty$. Since the length scale of the perturbations is then much less than that of fQ, a Taylor expansion of fQ is useful for the scales of interest. Then, in terms of Y, (2.1) becomes

$$\frac{\mathrm{d}^2\tilde{V}}{\mathrm{d}Y^2} + \frac{m^2L^2}{N^2}\left(\omega^2 - \overline{fQ} - LY\overline{(fQ)'} - \tfrac{1}{2}L^2Y^2\overline{(fQ)''} - \cdots\right)\tilde{V} = 0, \tag{2.4}$$

where the overbar denotes evaluation at $y = \overline{y}$. As $L \to 0$, localized solutions can be extracted from (2.4) provided $\overline{(fQ)'} = 0$ and $L \sim |m|^{-1/2} \to 0$. The optimal scaling between L and $|m|$ is

$$L = \left(\frac{1}{a|m|}\right)^{1/2}, \qquad a = \left(\frac{\overline{(fQ)''}}{2N^2}\right)^{1/2}, \tag{2.5a,b}$$

where a is a constant with dimensions of inverse length, introduced for convenience, in which case (2.4) becomes

$$\frac{\mathrm{d}^2\tilde{V}}{\mathrm{d}Y^2} + \left(\frac{\omega^2 - \overline{fQ}}{a^2N^2L^2} - Y^2\right)\tilde{V} = \frac{1}{a^2N^2}\left(\frac{L\overline{(fQ)'''}Y^3}{6} + \frac{L^2\overline{(fQ)''''}Y^4}{24} + \ldots\right)\tilde{V}. \tag{2.6}$$

With this formulation, the terms on the right-hand side of (2.6) are small compared with those on the left-hand side in the limit $L \to 0$, or equivalently as $|m| \to \infty$, at least when $Y \sim 1$. An approximate solution is thus obtained by setting the right-hand side of (2.6) to zero, and then (1.5) implies that solutions exist only when $\omega^2 - \overline{fQ} = (2n+1)a^2N^2L^2$, where n is a non-negative integer (e.g. Bender & Orszag 1978, p. 133). Using (2.5), we can equivalently write this eigencondition as $\omega^2 = \omega^2_{[1]}$, where

$$\omega^2_{[1]} = \overline{fQ} + \frac{(2n+1)N}{|m|}\left(\frac{\overline{(fQ)''}}{2}\right)^{1/2}. \tag{2.7}$$

The corresponding eigenmodes $\tilde{V}$ are proportional to $H_n(Y)$, where

$$H_n(x) = (-1)^n \mathrm{e}^{x^2/2}\frac{\mathrm{d}^n}{\mathrm{d}x^n}\left(\mathrm{e}^{-x^2}\right) \tag{2.8}$$

is the nth order Hermite function. Thus, from (1.2) and (2.3), the cross-stream flow is

$$\tilde{v} \sim H_n\left(\frac{y - \overline{y}}{L}\right)\mathrm{Re}\left(\overline{\omega}A\,\tilde{Z}(z)\mathrm{e}^{-\mathrm{i}\omega t}\right) \qquad \text{as } |m| \to \infty, \tag{2.9}$$

for some complex constant A, where $\overline{\omega}$ is the leading-order frequency, from (2.7):

$$\overline{\omega} = \pm(\overline{fQ})^{1/2}. \tag{2.10}$$

2.2. *Spatial structure of the solution*

Using Taylor expansions of f and Q about $y = \overline{y}$ in (1.1*a*,*c*), and substituting for m and a from (2.5), the remainder of the leading-order solution is

$$\tilde{u} \sim \overline{Q} H_n\left(\frac{y-\overline{y}}{L}\right) \mathrm{Re}\left(\mathrm{i}A\tilde{Z}(z)\mathrm{e}^{-\mathrm{i}\omega t}\right), \tag{2.11}$$

$$\tilde{\phi} \sim -\tfrac{1}{2}\overline{(fQ)''}L^3 H_n'\left(\frac{y-\overline{y}}{L}\right) \mathrm{Re}\left(\mathrm{i}A\tilde{Z}(z)\mathrm{e}^{-\mathrm{i}\omega t}\right). \tag{2.12}$$

With (2.9), this describes a shallow overturning motion in the (y, z)-plane with $n+1$ cells in the cross-stream direction, accompanied by $n+1$ jets in the along-stream direction, confined to a thin band of width $L \propto |m|^{-1/2}$ around $\overline{y}$, the minimum of fQ. From (2.5), the cross-stream scale L is also determined by the curvature of fQ at $y = \overline{y}$: a shallower minimum in fQ leads to a wider disturbance. For the $n = 0$ solution, which is the most unstable or has the lowest frequency, (2.8) and (2.9) imply that $\tilde{v} \propto \exp(-(y-\overline{y})^2/2L^2)$, so that the leading-order cross-stream structure is symmetric about $y = \overline{y}$.

The dynamical balance of (2.9), (2.11) and (2.12) is near-inertial, i.e. it involves negligible horizontal pressure gradients. The x-momentum balance is clearly inertial, since $\partial\tilde{\phi}/\partial x = 0$ when $k = 0$. In the y-momentum balance, (2.11) and (2.12) imply

$$\frac{\partial\tilde{\phi}/\partial y}{f\tilde{u}} \sim -\frac{\overline{(fQ)''}L^2}{2\overline{(fQ)}}\frac{H_n''}{H_n} = \frac{\overline{(fQ)''}L^2}{2\overline{\omega}^2}\left(2n+1-\left(\frac{y-\overline{y}}{L}\right)^2\right) \text{ as } |m| \to \infty. \tag{2.13}$$

Thus, in the region of large-amplitude motion where $|y-\overline{y}| \sim L$, the cross-stream pressure gradient becomes negligible compared to the Coriolis acceleration as $L \to 0$ (or $|m| \to \infty$), so that there is a purely inertial balance between $\partial\tilde{v}/\partial t$ and $f\tilde{u}$ in this limit. Thus, heuristic 'pressureless' parcel arguments (e.g. Holton 1992, § 7.5.1) are justified in the limit $|m| \to \infty$, when $L \sim |m|^{-1/2}$.

If $\overline{\omega}^2 = \overline{fQ} > 0$, the solutions are near-inertial waves, and (2.13) shows that the cross-stream pressure gradient reinforces the Coriolis acceleration near $y = \overline{y}$, leading to a greater restoring force and hence higher-frequency waves as $|m|$ decreases. If $\overline{\omega}^2 < 0$, the solutions are inertial instabilities, and the cross-stream pressure gradient opposes the Coriolis acceleration near $y = \overline{y}$, leading to a smaller destabilizing force and hence a lower growth rate as $|m|$ decreases. This stabilizing effect was noted for particular solutions by Dunkerton (1981, figure 1) and Stevens (1983, figure 6), but it generalizes to all other flows satisfying (2.2*a*–*c*). Indeed, it can be established from (2.1) using a variational approach, such as that used for a related problem by Griffiths (2003*a*, Appendix), that

$$\partial\omega^2/\partial|m| < 0, \qquad \omega^2 \to \min(fQ) \text{ as } |m| \to \infty. \tag{2.14a,b}$$

Thus, when $|m|$ falls below some value m_b, often referred to as a buoyancy cutoff wavenumber, the cross-stream pressure gradient renders the flow stable: $\omega^2 > 0$ for $|m| < m_b$. We can estimate m_b by setting $\omega_{[1]}^2 = 0$ in (2.7). Assuming that $Q \sim f$, and introducing λ as a length scale for fQ, we find that

$$m_b \sim (N/f)\lambda^{-1}. \tag{2.15}$$

For a flow with characteristic shear Λ on the equatorial β-plane, $fQ \approx \beta y(\beta y - \Lambda)$ implying a length scale $\lambda \sim \Lambda/2\beta$, so that $f \sim \beta\lambda \sim \Lambda/2$, and $m_b \sim 4N\beta/\Lambda^2$.

2.3. *The Rayleigh–Schrödinger perturbation expansions*

We can make the analysis more systematic by expanding ω^2 and $\tilde{V}$ as

$$\omega^2 \sim \omega_0^2 + (aL)^2\omega_1^2 + (aL)^4\omega_2^2 + \ldots, \quad \tilde{V}(y) \sim \tilde{V}_0(y) + aL\tilde{V}_1(y) + \ldots, \quad (2.16a,b)$$

substituting into (2.6), and gathering together terms of like order in L. The reasoning leading to (2.7) implies that

$$\omega_0^2 = \overline{fQ}, \quad \omega_1^2 = (2n+1)N^2, \quad \tilde{V}_0(y) = H_n(Y). \tag{2.17}$$

Equivalent expressions for ω_0^2 and ω_1^2 could be obtained by using the standard WKB expansion for a double turning-point eigenvalue problem (e.g. Bender & Orszag 1978, § 10.5), followed by a simplification to allow for the closeness of the turning points as $|m| \to \infty$, as in Billant & Gallaire (2005). However, the Rayleigh–Schrödinger perturbation approach is more direct, and higher-order corrections are more easily derived. The next-order terms in (2.16*a,b*) are derived in Appendix A: see (A5) and (A6). It turns out that only even powers of L are required in (2.16*a*).

Although it is simple to construct such expansions for almost arbitrary fQ, the analysis has one weakness: the 'perturbative' terms of the right-hand side of (2.6) are not small compared with those on the left-hand side when $Y \sim L^{-1}$. The perturbation problem is singular. The price we pay for the simplicity of the analysis is that (2.16*a,b*) are usually divergent for all L. However, they are asymptotic series for $\tilde{V}$ and ω^2 (e.g. Bender & Orszag 1978, § 3.8), and useful information can still be extracted provided (2.2*a–c*) are satisfied (n.b. it is necessary that $\overline{y}$ be the global minimum of fQ, although this was not apparent in § 2.1). Then, it is possible to study how such series may be optimally truncated (e.g. Toloza 2001) or Padé resummed (e.g. Sergeev & Goodson 1998). The archetypal problem illustrating these concepts is that of the quantum anharmonic oscillator (e.g. Bender & Orszag 1978, § 7; Bender & Bettencourt 1996).

Since we derive only the first three terms of (2.16*a,b*), we will simply evaluate the utility of the truncated series

$$\omega_{[J]}^2 = \sum_{j=0}^{J}(aL)^{2j}\omega_j^2, \qquad \tilde{V}_{[J]}(y) = \sum_{j=0}^{J}(aL)^j\tilde{V}_j(y) \qquad (J = 0, 1, 2). \tag{2.18}$$

Even though the full series may be divergent, we expect (2.18) to be useful approximations when the cross-stream scale separation underlying the analysis is satisfied, i.e. when

$$L \ll \lambda, \text{ where } \lambda \text{ is a length scale for the flow.} \tag{2.19}$$

The first non-trivial approximation for ω^2 is (2.7), which is consistent with (2.14*a,b*). However, higher-order approximations are not guaranteed to satisfy (2.14*a*). For instance, if ω_2^2 is negative then $\partial\omega_{[2]}^2/\partial|m| > 0$ for sufficiently small $|m|$, and it is more natural to use the [1/1] Padé approximant (e.g. Bender & Orszag 1978, § 8.3):

$$\omega_{[1/1]}^2 = \frac{\omega_0^2 + (aL)^2\left(\omega_1^2 - \omega_0^2\omega_2^2/\omega_1^2\right)}{1 - (aL)^2\omega_2^2/\omega_1^2}. \tag{2.20}$$

This agrees with (2.16*a*) up to terms of order L^4, and satisfies (2.14*a,b*).

2.4. *Example: shear layer on an f-plane*

Consider the family of shear flows given by

$$U = f\lambda Ro\,\tanh(y/\lambda), \qquad fQ = f^2\left(1 - Ro\,\mathrm{sech}^2(y/\lambda)\right), \tag{2.21}$$

with f constant, $\lambda > 0$, and $Ro > 0$ to satisfy (2.2*b*,*c*). This is a particularly useful case to examine because the eigenvalues, for (1.5) and (2.1), can be determined exactly (e.g. Bender & Orszag 1978, p. 28):

$$\omega^2 = -f^2\left(Ro - 1 - (2n+1)\frac{m_f}{|m|}\left(Ro + \frac{m_f^2}{4m^2}\right)^{1/2} + \left(n^2 + n + \frac{1}{2}\right)\frac{m_f^2}{m^2}\right). \tag{2.22}$$

Here $m_f = (N/|f|)\lambda^{-1}$, and n is any integer satisfying

$$0 \leqslant n \leqslant \tfrac{1}{2}\left[\left(1 + 4Ro\,(m/m_f)^2\right)^{1/2} - 1\right],$$

so that there are only a finite number of discrete eigenvalues. As $|m|$ decreases, the number of discrete solutions decreases, although the $n = 0$ solution exists for all $|m|$, with $\omega^2 \to f^2$ as $|m| \to 0$. When $0 < Ro \leqslant 1$, (2.22) describes inertia–gravity waves. When $Ro > 1$, there is a region with $fQ < 0$, and (2.22) describes an inertial instability when $|m| > m_b$, where

$$m_b = (Ro - 1)^{-1}(N/|f|)\lambda^{-1}. \tag{2.23}$$

This is consistent with the scaling of (2.15).

We apply the asymptotic analysis of § 2.3 by setting $\overline{y} = 0$ in (2.5), giving

$$L = Ro^{-1/4}\left(\frac{N}{|f|}\frac{\lambda}{|m|}\right)^{1/2} = \lambda\, Ro^{-1/4}\left(\frac{m_f}{|m|}\right)^{1/2}, \tag{2.24}$$

whilst (2.16*a*), (2.17) and (A6) then give

$$\omega^2 \sim -f^2\left(Ro - 1 - (2n+1)Ro^{1/2}\frac{m_f}{|m|} + \left(n^2 + n + \frac{1}{2}\right)\frac{m_f^2}{m^2} + \ldots\right), \tag{2.25}$$

as $|m| \to \infty$. Comparing with (2.22), it is clear that (2.25) recovers the correct behaviour as $|m| \to \infty$. Since $\omega_2^2 < 0$, the best truncated approximation to use is $\omega_{[1/1]}^2$, given by (2.20). For the $n = 0$ eigenmode, it can be shown that (i) $\omega_{[1/1]}^2 - \omega^2$ is positive and monotonically decreases as $|m|$ increases, so that the maximum error occurs at $|m| = 0$, with value $Ro\,f^2$; (ii) if $1 < Ro \leqslant 2$, then $|\omega_{[1/1]}^2 - \omega^2| < 0.05f^2$ over the unstable region. Thus, even though (2.19) and (2.24) imply a scale separation only when $|m| \gg Ro^{-1/2}m_f$, $\omega_{[1/1]}^2$ is accurate for $|m|$ of order m_f.

This example illustrates two limitations of the analysis. First, it gives infinitely many discrete eigenvalues, whereas there are only a finite number for cases such as (2.21) with $(fQ)_\infty$ bounded. However, this is not a concern if we are interested only in the most unstable (or lowest frequency) eigenmode, which is obtained by setting $n = 0$. Secondly, (2.1) and (2.21) show that discrete eigenmodes $\tilde{V}(y)$ behave as $\exp(-|m|(f^2 - \omega^2)^{1/2}|y|/N)$ for large $|y|$, whilst the leading-order solution (2.9) behaves as $\exp(-y^2/2L^2)$. Bender & Bettencourt (1996) discuss a similar disparity, and show how such differences can be resolved by considering higher-order terms of the expansion. However, the large-amplitude behaviour of $\tilde{V}(y)$, near $y = 0$, is predicted well by the leading-order solution.

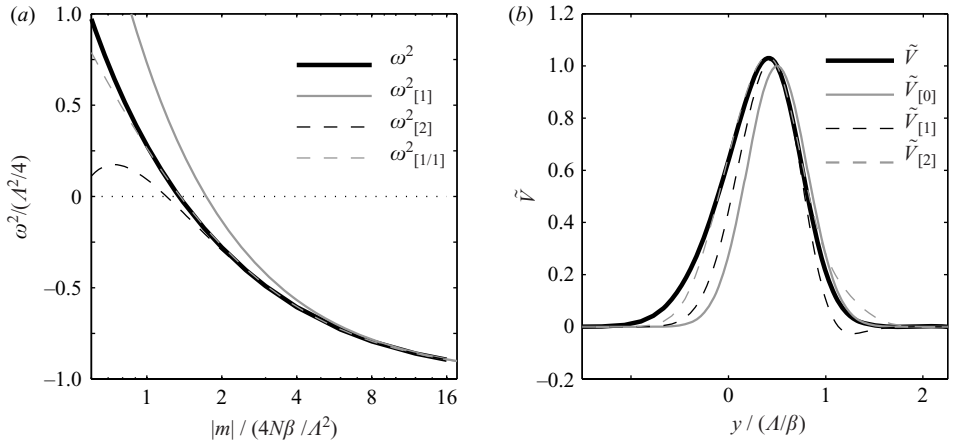

FIGURE 2. (*a*) Numerically determined and analytically estimated eigenvalues ω^2 for the symmetric ($k = 0$) instability of profile (2.26) at $\alpha = 1$. (*b*) Corresponding cross-stream structure $\tilde{V}(y)$ at $|m| = 6N\beta/\Lambda^2$, normalized so that $\tilde{V} = 1$ at $y = \Lambda/2\beta$.

2.5. *Example: shear layer on the equatorial β-plane*

We now consider flows on the equatorial β-plane, and thus set $f = \beta y$. Exact solutions are available for flows with uniform shear (Dunkerton 1981) or linear shear (Stevens 1983), both of which are recovered by (2.7) and (2.9), since all higher-order corrections vanish. Here we consider a set of shear layers with finite width λ and maximum shear Λ:

$$U(y) = \lambda\Lambda \tanh\left((y - \Lambda/2\beta)/\lambda\right). \tag{2.26}$$

Each flow is characterized by a single non-dimensional parameter $\alpha = \Lambda/(2\beta\lambda)$, with the uniform shear case recovered as $\alpha \to 0$.

To apply the asymptotic analysis of § 2.3, we note that fQ has a minimum at $\overline{y} = \Lambda/2\beta$, with $\overline{fQ} = -\Lambda^2/4$, and $\overline{(fQ)''} = 2\beta^2 + \Lambda^2/\lambda^2$. This turns out to be the global minimum, so that (2.5) gives

$$L = (1 + 2\alpha^2)^{-1/4}(N/\beta|m|)^{1/2}, \tag{2.27}$$

whilst (2.16*a*), (2.17) and (A6) give

$$\omega^2 \sim -\frac{\Lambda^2}{4}\left(1 - \left(1 + 2\alpha^2\right)^{1/2}\frac{m_\beta}{|m|} + \frac{\alpha^4\left(15 + 8\alpha^2\right)}{4(1 + 2\alpha^2)^2}\frac{m_\beta^2}{m^2} + \ldots\right), \qquad m_\beta = \frac{4N\beta}{\Lambda^2}, \tag{2.28}$$

as $|m| \to \infty$. Since $\overline{fQ} < 0$, the flow is unstable for sufficiently large $|m|$, so we have set $n = 0$ in (2.28) to obtain the most unstable eigenmode. Compared to the uniform shear limit $\alpha = 0$, at $\alpha \neq 0$ the instability has a smaller growth rate, a smaller latitudinal scale, and a larger buoyancy cutoff wavenumber: $m_b \approx (1 + 2\alpha^2)^{1/2}4N\beta/\Lambda^2$, based on $\omega^2_{[1]}$. Even though $\overline{fQ}$ is independent of α, when $\alpha \neq 0$ the flow is less unstable at finite $|m|$ since the shear layer is of limited extent.

We evaluate the accuracy of the asymptotic analysis by comparing with numerical calculations of the most unstable eigenmode, obtained as described in Appendix B. Typical results, at $\alpha = 1$, are shown in figure 2(*a*), along with the predictions obtained from (2.28). We can see that $\omega^2_{[1]}$, $\omega^2_{[2]}$ and $\omega^2_{[1/1]}$ recover the correct limiting behaviour of ω^2 at large $|m|$. Since the coefficient of $|m|^{-2}$ in (2.28) is negative, $\omega^2_{[2]}$ eventually

decreases for sufficiently small $|m|$, and $\omega^2_{[1/1]}$ is clearly the best approximant. Using (2.27), the scale separation condition (2.19) reduces to $|m| \gg 4N\beta/\Lambda^2$ when α is of order unity, but $\omega^2_{[1/1]}$ is accurate to within $0.02 \times \Lambda^2/4$ even when $|m| = 4N\beta/\Lambda^2$.

Shown in figure 2(*b*) is the latitudinal structure of the most unstable eigenmode at $\alpha = 1$ and $|m| = 6N\beta/\Lambda^2$, close to the buoyancy cutoff, where $L/\lambda = 2^{1/2}/3^{3/4} = 0.62$. Whilst the leading-order prediction $\tilde{V}_{[0]}$ is symmetric about $\overline{y} = \Lambda/2\beta$, $\tilde{V}(y)$ is asymmetric, and part of this asymmetry is captured by $\tilde{V}_{[1]}$ and $\tilde{V}_{[2]}$. The maximum absolute errors for $\tilde{V}_{[0]}$, $\tilde{V}_{[1]}$ and $\tilde{V}_{[2]}$ are 0.37, 0.22 and 0.08, respectively. Convergence is slower for $\tilde{V}(y)$ than it is for ω^2, since from (2.16*b*) corrections for $\tilde{V}(y)$ are only proportional to $|m|^{-1/2}$.

3. Non-symmetric solutions

We now turn to the main problem of interest: determination from (1.3) of the frequency ω and structure of the near-inertial eigenmodes when $k \neq 0$. Although this is considerably more complex than the problem with $k = 0$, we again seek localized solutions with a simple Rayleigh–Schrödinger perturbation expansion. This generalizes and extends the analysis of Clark & Haynes (1996), who used similar methods to determine the stability of an equatorial flow with uniform latitudinal shear. There are also similarities to a stability analysis of quasi-geostrophic flow by Killworth (1980, § 8). We shall focus on unstable flows for which the imaginary part of ω is non-zero, so that (1.3) has no singularities.

Throughout this section we shall make frequent comparison with the results of Billant & Gallaire (2005), who solved the corresponding problem for flows with circular symmetry. Although they used a somewhat different approach (a WKB expansion), their results are closely related to those given here.

3.1. *The small-k regime*

We start by illustrating some generic properties of the non-symmetric eigenmodes by considering their form at small k and large $|m|$. As in § 2, we suppose that there is a streamline $y = \overline{y}$ at which fQ has a global minimum, and that the solutions have a small cross-stream length scale L. The leading-order terms in k and m can then be obtained by setting $k \sim L \sim |m|^{-1/2}$, and considering the limit $|m| \to \infty$. We use (2.16*b*) for $\tilde{V}(y)$, but for ω we write

$$\omega - k\overline{U} \sim \omega_0 + (aL)^2\omega_1 + \ldots. \tag{3.1}$$

Our construction is based upon the $k = 0$ solutions, and thus we must have $\omega_0 = \overline{\omega} = \pm\left(\overline{fQ}\right)^{1/2}$, where $\overline{\omega}$ is the leading-order (imaginary) frequency at $k = 0$. Then, introducing a rescaled coordinate Y according to (2.3) and (2.5), (1.3) becomes

$$\frac{\mathrm{d}^2\tilde{V}_0}{\mathrm{d}Y^2} + \left(\frac{2\overline{\omega}\omega_1}{N^2} - \frac{4\overline{\omega}\overline{U'}}{\overline{(fQ)''}}\left[\frac{k}{L}\right]Y - Y^2\right)\tilde{V}_0 = O(L), \tag{3.2}$$

where we have used Taylor series for $U(y)$ and $(fQ)(y)$ around $y = \overline{y}$. In the coefficient of $\tilde{V}$ in (1.3), the only terms which contribute to (3.2) at leading order come from $\hat{\omega}^2 - fQ$.

Equation (3.2) reduces to the parabolic cylinder equation when written in terms of $Y + 2\overline{\omega}kL^{-1}\overline{U'}/\overline{(fQ)''}$. Thus, using (2.3), for solutions satisfying (1.5) we find

$$\tilde{V}_0 = H_n\left(\frac{y - \overline{y}_k}{L}\right), \qquad \overline{y}_k = \overline{y} - 2k\overline{\omega}\overline{U'}/\overline{(fQ)''}, \tag{3.3a,b}$$

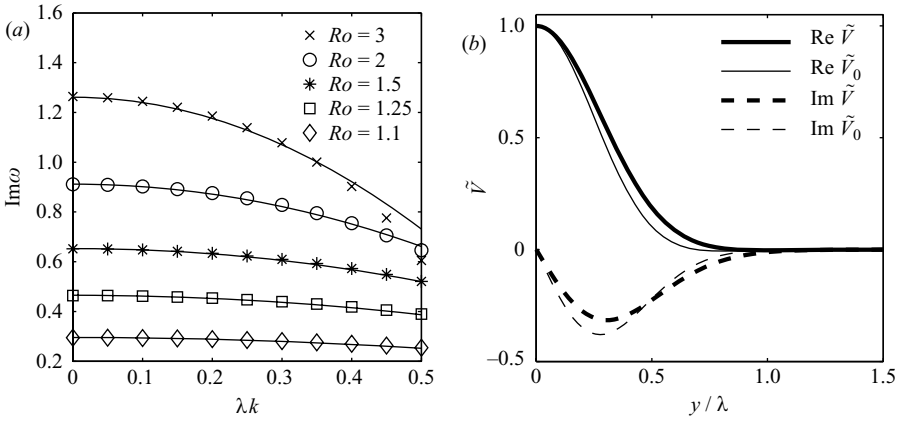

FIGURE 3. Inertial instability of the hyperbolic-tangent velocity profile (2.21) at small k. (a) Growth rates (symbols) at $|m| = 8m_b$, with m_b given by (2.23), along with the theoretical predictions (solid lines) determined from (3.5). (b) Cross-stream structure at $Ro = 2$, $k = 0.2\lambda^{-1}$ and $|m| = 8m_b = 8(N/|f|)\lambda^{-1}$, along with theoretical predictions determined from (3.6a).

and a corresponding eigencondition for ω_1. Substituting into (3.1), the series for ω starts

$$\omega \sim k\overline{U} \pm (\overline{fQ})^{1/2}\left(1 + \frac{(2n+1)N}{2|m|(\overline{fQ})}\left(\frac{\overline{(fQ)''}}{2}\right)^{1/2} - \frac{k^2\overline{U'^2}}{\overline{(fQ)''}} + \ldots\right), \tag{3.4}$$

using (2.5) and (2.10), where $k \to 0$ and $|m| \to \infty$. Thus, for the growing mode, the growth rate decreases as $|k|$ increases from zero. Billant & Gallaire (2005) reported a corresponding result for flows with circular symmetry.

From (3.3a), the eigenmodes are now centred at $\overline{y}_k$ rather than $\overline{y}$. However, from (3.3b), $\overline{y}_k$ is complex, since $\overline{\omega}$ is imaginary, so that the eigenmodes are apparently centred at a complex streamline. This is consistent with the results of Billant & Gallaire (2005), in which stability was determined by properties evaluated at a complex radius. Although the use of a complex streamline is somewhat alarming, stability calculations often require physical space to be immersed in the complex plane, which is perhaps related to the introduction of the Fourier representation (1.2). There is a strong analogy here with absolute instability calculations (e.g. Chomaz, Huerre and Redekopp 1991), where growth rates are determined by evaluating a dispersion relation at a spatial location in the complex plane.

Nevertheless, to check that these solutions do have physical relevance, we return to the flow of § 2.4 and calculate ω numerically for the $n = 0$ eigenmode over $0 \leqslant \lambda k \leqslant 0.5$ and $1 < Ro \leqslant 3$ (we shall have more to say about how these solutions are calculated in § 4). The results are shown in figure 3(a). Also shown are the predictions of (3.4) with $n = 0$, which using (2.21) with $\overline{y} = 0$ becomes

$$\omega \sim \pm \mathrm{i} f\,(Ro-1)^{1/2}\left(1 - \frac{Ro^{1/2}}{2(Ro-1)}\frac{N}{f\lambda|m|} - \frac{Ro\lambda^2k^2}{2} + \ldots\right). \tag{3.5}$$

Figure 3(a) shows that (3.5) captures the variations of ω with k, at least for sufficiently large $|m|$, so that the use of a complex streamline $\overline{y}_k$ is justified.

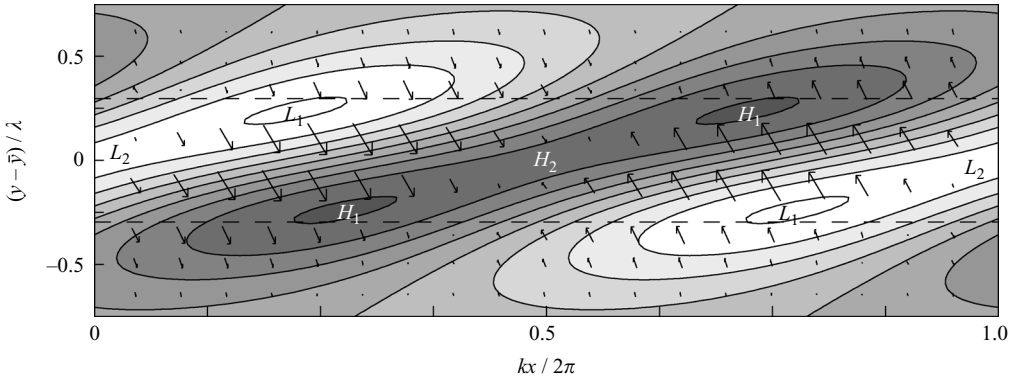

FIGURE 4. Horizontal structure of the non-symmetric inertial instability. Contoured is the pressure perturbation: white is negative, dark grey is positive. The arrows indicate the horizontal velocity vector, the length of the arrow being proportional to $\sqrt{\tilde{u}^2+\tilde{v}^2}$. The x-component of each arrow has been enhanced by a factor of 5 relative to the y-component. The two horizontal dashed lines are $y=\overline{y}\pm L$.

3.2. *Spatial structure of the solution*

The need for $\overline{y}_k$ to be complex reflects a change in the spatial structure of the solutions from that at $k=0$. For instance, normalizing the $n=0$ eigenmode so that $\tilde{V}=1$ at $y=\overline{y}$, (2.8) and (3.3*a*,*b*) give

$$\tilde{V}\sim\tilde{V}_0=\exp\left\{-\frac{(y-\overline{y})^2}{2L^2}\right\}\exp\{\mathrm{i}l(y-\overline{y})\},\quad l=\frac{2\mathrm{i}k\overline{\omega}\overline{U'}}{L^2\overline{(fQ)''}}. \tag{3.6a,b}$$

Here, l is a real cross-stream wavenumber, since $\overline{\omega}$ is imaginary. Thus, at fixed x, z and t, the most unstable eigenmode has cross-stream oscillations modulated by a Gaussian envelope. This is confirmed in figure 3(*b*), where (3.6*a*) is compared with a numerically determined solution corresponding to a case shown in figure 3(*a*). The largest values of $|\tilde{V}|$ are associated with $\mathrm{Re}\,\tilde{V}$, which is symmetric about $y=\overline{y}$, with limiting form $\cos(l(y-\overline{y}))\exp(-(y-\overline{y})^2/2L^2)$. At small k, the modulating Gaussian envelope ensures that the oscillations in $\tilde{V}$ for $|y-\overline{y}|>\pi/2l$ are invisible. In contrast, $\mathrm{Im}\,\tilde{V}$ is asymmetric about $y=\overline{y}$, with limiting form $\sin(l(y-\overline{y}))\exp(-(y-\overline{y})^2/2L^2)$. However, at small k, the modulating Gaussian envelope renders this weak relative to the symmetric pattern of $\mathrm{Re}\,\tilde{V}$.

The wavenumbers k and l imply the appearance of phase lines in the horizontal and vertical structure of the solution. For instance, for the $n=0$ eigenmode, the horizontal velocities can be written as

$$\begin{pmatrix}\tilde{u}\\ \tilde{v}\end{pmatrix}\sim\exp\left\{-\frac{(y-\overline{y})^2}{2L^2}\right\}\mathrm{Re}\left\{\begin{pmatrix}\mathrm{i}\overline{Q}\\ \overline{\omega}\end{pmatrix}A\exp(\mathrm{i}(kx+l(y-\overline{y})-\omega t)\tilde{Z}(z)\right\}, \tag{3.7a,b}$$

to leading order as $k\to 0$ and $|m|\to\infty$, using (1.1*a*), (1.2) and (3.6*a*), for some complex constant A. This pattern is illustrated in figure 4, which was generated from the numerical solution of figure 3(*b*). The largest velocities (at $kx=\pi/2$ and $kx=3\pi/2$) have cross-stream symmetry, although a weaker pattern with cross-stream asymmetry also exists (at $kx=\pi$). This is in contrast to the picture at $k=0$, where to leading order $\tilde{u}$ and $\tilde{v}$ are always symmetric about $y=\overline{y}$ for the most unstable eigenmode, being simply the Gaussian envelope of (3.7*a*,*b*) with $k=l=0$.

Where the strong horizontal flow dies out or reverses, there are regions of horizontal divergence, producing the pattern of pressure perturbations contoured in figure 4. For instance, at the points marked H_1 and H_2, there must be upward flow (and positive density perturbations) aloft and downward flow (and negative density perturbations) beneath, implying local pressure maxima. The converse applies at the points L_1 and L_2. Since $\partial\tilde{v}/\partial y \sim \tilde{v}/L$ and $\partial\tilde{u}/\partial x \sim k\tilde{u}$, and $\tilde{u} \sim \tilde{v}$, the horizontal divergence is mainly generated by $\partial\tilde{v}/\partial y$, so that the pressure perturbations are largest near $kx = \pi/2$ and $kx = 3\pi/2$, and are approximately asymmetric about $y = \overline{y}$. The horizontal divergence generated by $\partial\tilde{u}/\partial x$ and the asymmetric part of $\tilde{v}$ leads to a weaker pattern with cross-stream symmetry at $kx = \pi$. Dunkerton (1983, § 3e) has also discussed the horizontal structure of non-symmetric solutions in similar terms, but for rather different parameters.

It is clear from figure 4 that both the cross-stream pressure gradients (from H_1 to L_1) and the along-stream pressure gradients (from H_2 to L_2) oppose the horizontal motion of the instability. We evaluate the degree to which these horizontal pressure gradients enter the dynamical balance, relative to the inertial terms which are dominant as $|m| \to \infty$ at $k = 0$. For the $n = 0$ eigenmode, (1.1*a*), (2.5) and (3.7*b*) imply

$$\tilde{\phi} \sim \tfrac{1}{2}\overline{(fQ)''}L^3 \exp\left(-\frac{(y-\overline{y})^2}{2L^2}\right) \times \mathrm{Re}\left(\left(\frac{\mathrm{i}(y-\overline{y})}{L} + \frac{2\mathrm{i}k\overline{\omega}\overline{U'}}{L\overline{(fQ)''}}\right) A \exp(\mathrm{i}(kx + l(y-\overline{y}) - \omega t))\tilde{Z}(z)\right). \quad (3.8)$$

Thus, using (3.7*b*), $\partial\tilde{\phi}/\partial x = -k^2L^2\overline{U'}\tilde{v}$ at $y = \overline{y}$, so that in the along-stream momentum balance $-(\partial\tilde{\phi}/\partial x)/(Q\tilde{v}) = -k^2L^2(1 - \overline{f/Q})$ at $y = \overline{y}$. Thus, as already noted graphically, at the centre of the unstable region the along-stream pressure gradient opposes the inertial term $Q\tilde{v}$, since $\overline{f/Q} < 0$. However, since the pressure-gradient scales as k^2L^2 relative to the inertial terms, it is insignificant for small k and L. More significant is the cross-stream pressure gradient, for which (2.5), (3.6) and (3.8) imply

$$\left.\frac{\partial\tilde{\phi}/\partial y}{f\tilde{u}}\right|_{y=\overline{y}} \sim \frac{N}{|m|\overline{(fQ)}}\left(\frac{\overline{(fQ)''}}{2}\right)^{1/2} - \frac{2k^2\overline{U'}^2}{\overline{(fQ)''}}. \quad (3.9)$$

The term $\propto N/|m|$, which opposes the Coriolis acceleration since $\overline{fQ} < 0$, is the leading-order effect of buoyancy, and has already been discussed in (2.13). The term $\propto k^2$, which is the leading-order effect of along-stream asymmetries, also opposes the Coriolis acceleration. Thus, the along-stream asymmetries act to increase the cross-stream pressure gradient, which opposes the destabilizing Coriolis acceleration and thus reduces the growth rate of the inertial instabilities. Note the consistency of this analysis with (3.4), in which the corrections to the leading-order frequency $\overline{\omega}$ for the $n = 0$ eigenmode are proportional to (3.9). Repeating the calculation (3.9) for the nth eigenmode, using (A2) for H_n'', leads to an additional factor $(2n + 1)$ to make the correspondence exact.

Although these conclusions only hold for sufficiently small k and large $|m|$, they can be used to anticipate results for larger k and smaller $|m|$. In particular, we anticipate that when k approaches some value k_c, which we might call a short-wave cutoff wavenumber, the cross-stream pressure-gradient associated with the along-stream asymmetries can completely stabilize the flow. This is analogous to the buoyancy cutoff for the vertical wavenumber introduced in § 2.1. We can estimate the magnitude of k_c by considering when the term of (3.4) purely associated with along-stream

asymmetries becomes comparable to the leading-order growth rate. If $U' \sim f$ and fQ has length scale λ, this occurs when $k^2 \sim \overline{(fQ)''}/\overline{U'^2} \sim (f^2/\lambda^2)/f^2 \sim \lambda^{-2}$, implying

$$k_c \sim \lambda^{-1}. \tag{3.10}$$

For flows on the equatorial β-plane, for which $\lambda \sim \Lambda/\beta$, we thus expect $k_c \sim \beta/\Lambda$.

3.3. *The general analysis*

We now consider the most general case with no *a priori* restrictions on k. Since in § 3.1 the centring of the modes became k-dependent, we introduce a general rescaled and shifted cross-stream coordinate Y defined via

$$Y = \frac{y - \overline{y}_k}{L_k}, \quad L_k = \left(\frac{1}{a_k|m|}\right)^{1/2}. \tag{3.11a,b}$$

Here $\overline{y}_k$ and a_k will depend on k but are independent of m, and will be determined as part of the analysis. In terms of Y, the governing equation (1.3) becomes

$$L_k^2 \frac{\mathrm{d}^2\tilde{V}}{\mathrm{d}Y^2} + \left(\frac{2L_k^3 k\hat{\omega}U'}{\hat{\omega}^2 - L_k^4 N^2 a_k^2 k^2}\right)\frac{\mathrm{d}\tilde{V}}{\mathrm{d}Y} + \left(\frac{\hat{\omega}^2 - fQ}{a_k^2 N^2} - L_k^4\left(k^2 + \frac{kQ'}{\hat{\omega}} + \frac{2k^2 QU'}{\hat{\omega}^2 - L_k^4 N^2 a_k^2 k^2}\right)\right)\tilde{V} = 0. \tag{3.12}$$

Once again we shall seek solutions in the limit $L_k \to 0$, and thus make Taylor expansions about $y = \overline{y}_k$ for f, U and Q in (3.12). We also introduce perturbation expansions

$$\omega - k\overline{U_k} \sim \omega_0 + (a_k L_k)^2\omega_1 + (a_k L_k)^4\omega_2 + \ldots, \tag{3.13}$$

$$\tilde{V}(y) \sim \tilde{V}_0(Y) + (a_k L_k)\,\tilde{V}_1(Y) + (a_k L_k)^2\,\tilde{V}_2(Y) + \ldots, \tag{3.14}$$

where $\overline{U_k} = U(\overline{y}_k)$.

Gathering together terms of like order in L_k in (3.12), it is apparent that the $\hat{\omega}^2 - fQ$ term determines the low-order behaviour. Using (1.4) and (3.13), we have

$$\hat{\omega}^2 - fQ = \omega_0^2 - \overline{(fQ)_k} - L_k\left(2k\omega_0\overline{U_k'} + \overline{(fQ)_k'}\right)Y + L_k^2\left(2a_k^2\omega_0\omega_1 - \left(\tfrac{1}{2}\overline{(fQ)_k''} + k\omega_0\overline{U_k''} - k^2\overline{U_k'}^2\right)Y^2\right) + O(L_k^3). \tag{3.15}$$

Thus, since $\tilde{V}_0(Y)$ is not identically zero, the leading-order terms of (3.12), of $O(1)$, imply

$$\omega_0^2 - \overline{(fQ)_k} = 0. \tag{3.16a}$$

By the same reasoning, the next-order terms of (3.12), of $O(L_k)$, yield

$$2k\omega_0\overline{U_k'} + \overline{(fQ)_k'} = 0. \tag{3.16b}$$

The coupled system (3.16*a*,*b*) may be solved to give $\overline{y}_k$ and ω_0 in terms of k. The next order terms of (3.12), of $O(L_k^2)$, may be simplified by choosing

$$a_k = \left(\frac{\overline{(fQ)_k''} + 2k\omega_0\overline{U_k''} - 2k^2\overline{U_k'}^2}{2N^2}\right)^{1/2} \qquad (-\pi/2 < \arg a_k \leqslant \pi/2). \tag{3.17}$$

In (3.11*b*), the square root is taken in a similar manner, so that $-\pi/4 \leqslant \arg L_k < \pi/4$. Then, using (3.15), the relevant terms of (3.12) are

$$\frac{\mathrm{d}^2\tilde{V}_0}{\mathrm{d}Y^2} + \left(\frac{2\omega_0\omega_1}{N^2} - Y^2\right)\tilde{V}_0 = 0, \qquad \tilde{V}_0 \to 0 \text{ as } Y \to \pm\arg(L_k)\infty,$$

the boundary conditions following from (1.5) and (3.11*a*). If $\arg(a_k) = \pi/2$, then there are no solutions with $\tilde{V}_0$ and $\mathrm{d}\tilde{V}_0/\mathrm{d}Y$ decaying as $|y| \to \infty$, as may be shown by considering the asymptotic behaviour as $|Y| \to \infty$ of the parabolic cylinder functions (e.g. Bender & Orszag 1978, pp. 131–133). Otherwise, that is if

$$\arg\left(\overline{(fQ)}''_k + 2k\omega_0\overline{U}''_k - 2k^2\overline{U}'^2_k\right) \neq \pi, \tag{3.18}$$

there are solutions for $\tilde{V}_0$ and an eigencondition for ω_1:

$$\tilde{V}_0 = H_n(Y), \qquad \omega_1 = \frac{(2n+1)N^2}{2\omega_0}. \tag{3.19a,b}$$

Here n is a non-negative integer, and the Hermite functions are defined by (2.8).

Thus, using (3.11*b*), (3.17) and (3.19*b*), the first two terms of (3.13) are

$$\omega \sim k\overline{U}_k + \omega_0 + \frac{(2n+1)N}{2\omega_0|m|}\left(\tfrac{1}{2}\overline{(fQ)}''_k + k\omega_0\overline{U}''_k - k^2\overline{U}'^2_k\right)^{1/2} + \ldots, \tag{3.20}$$

whilst from (1.2), (3.11*a*) and (3.19*a*) the leading-order cross-stream flow is

$$\tilde{v} \sim \mathrm{Re}\left(\overline{\omega}AH_n\left(\frac{y-\overline{y}_k}{L_k}\right)\tilde{Z}(z)\exp\left(\mathrm{i}(kx-\omega t)\right)\right), \tag{3.21}$$

for some complex constant A, as $|m| \to \infty$. It is simple, albeit lengthy, to calculate the next terms in both series. The procedure is illustrated in Appendix A for the $n = 0$ eigenmode, yielding (A10) for $\tilde{V}_1$ and (A12) for ω_2.

3.4. *Structure of the expansions*

Construction of this solution relied upon three conditions. Two of these, (3.16*a*,*b*), are solved to give $\overline{y}_k$ and ω_0 in terms of k. The third condition, (3.18), then amounts to a condition on k for eigenmodes of this form to exist. When $k = 0$, the three conditions can be satisfied by choosing $\overline{y}_k$ to be a minimum of fQ. However, when $k \neq 0$, the conditions are more difficult to solve. Further, if we suppose that a solution $\overline{y}_k$ is real, then, in general, (3.16*b*) implies that ω_0 is real, so that from (3.13) ω is also real to leading order in $|m|^{-1}$. Thus for instability at leading order with $k \neq 0$, $\overline{y}_k$ will have an imaginary part. This is consistent with the small k expansion (3.3*b*), and appears to be necessary so that the solutions can be represented in terms of Hermite functions.

When $k = 0$, for the asymptotic series to be useful $\overline{y}_k$ must be the global minimum $\overline{y}$ of fQ. This was not apparent in the analysis of § 2.3, and by analogy we expect there to be a similar hidden global criterion when $k \neq 0$. This is a concern, because (3.16*a*,*b*) typically lead to at least two values for $\overline{y}_k$. Therefore we consider only solutions for which

$$\overline{y}_k \to \overline{y} \text{ as } k \to 0. \tag{3.22}$$

As already shown in (3.3*b*), for small k there exist two such solutions for $\overline{y}_k$, and we assume that their extensions to finite k are physically meaningful. These solutions are a natural extension of the symmetric inertial instabilities obtained at $k = 0$ to fully three-dimensional inertial instabilities with $k \neq 0$.

Unlike the analysis of § 2.3, for which the Rayleigh–Schrödinger perturbation series have well-established properties, there seems to be little mathematical foundation for a corresponding complex analysis. However, our predictions are consistent with those which would be obtained by using a more rigorous complex WKB method, such as that used by Billant & Gallaire (2005). We justify our approach by showing that it produces results consistent with numerically determined solutions. We shall analyse unstable flows, and evaluate the growth rate σ and the intrinsic phase speed c at $y = \overline{y}$, defined via

$$\sigma = \mathrm{Im}(\omega), \qquad c = \left(\mathrm{Re}(\omega) - k\overline{U}\right)/k. \tag{3.23}$$

We evaluate the accuracy of truncated versions of (3.13):

$$\sigma_{[J]} = \mathrm{Im}\left(k\overline{U_k} + \sum_{j=0}^{J} (a_k L_k)^{2n}\, \omega_n\right), \tag{3.24}$$

with a corresponding expression for $c_{[J]}$. As before, we expect these approximations to be useful when the scale separation underlying the analysis is satisfied, i.e. when $L_k \ll \lambda$, where λ is a length scale for the flow. From (3.11), this will be assured when $|m|$ is sufficiently large, but just how large will depend on $a_k(k)$. To maintain the ordering in (3.20), we also require ω_0 to be of order unity, which must be checked case-by-case.

4. Instability of a shear layer on the f-plane

We return to the family of flows (2.21), corresponding to an anticyclonic shear layer on the f-plane. Here $\lambda > 0$ is the width of the shear layer, and $Ro > 0$ is a Rossby number for the flow. When $m = 0$, (1.3) yields a barotropic Kelvin–Helmholtz instability when $\lambda|k| < 1$, with a maximum growth rate of $0.19 \times$ the maximum shear (Michalke 1964), i.e. $0.19\,|f|Ro$ when applied to (2.21). In contrast, when $k = 0$, (2.22) implies an inertial instability when $Ro > 1$ and $|m| > m_b = (Ro-1)^{-1}(N/|f|)\lambda^{-1}$, with a maximum growth rate of $|f|(Ro-1)^{1/2}$. Thus, the inertial instability is expected to be stronger than the Kelvin–Helmholtz instability when $Ro \gtrsim 1.05$, provided $|m|$ can become sufficiently large (cf. the comments in § 4 of Stevens & Ciesielski 1986, the numerical simulations of Shen & Evans 2002, and the results in § 5 of Billant & Gallaire 2005). At $Ro = 2$, the $k = 0$ inertial instability is the strongest possible normal-mode instability: $\sigma \to |f|$ as $|m| \to \infty$, the maximum attainable value from (1.6).

4.1. *Limiting solutions*

The small k theory of § 3.1 has already been applied to this flow, yielding (3.5). Now we apply the theory of § 3.3 to obtain more general expressions for three-dimensional inertial instabilities. Equations (3.16*a*,*b*) lead to

$$\omega_0 = \pm f\left(\frac{1-Ro}{1-Ro\lambda^2k^2}\right)^{1/2}, \quad \tanh\left(\frac{\overline{y}_k}{\lambda}\right) = \mp\lambda k\left(\frac{1-Ro}{1-Ro\lambda^2k^2}\right)^{1/2}, \tag{4.1}$$

and then (3.11*b*) and (3.17) give

$$a_k = \frac{|1-\lambda^2k^2|}{\left(Ro^{-1}-\lambda^2k^2\right)^{1/2}}\frac{|f|}{N\lambda}, \qquad L_k = \frac{\left(Ro^{-1}-\lambda^2k^2\right)^{1/4}}{|1-\lambda^2k^2|^{1/2}}\left(\frac{N\lambda}{|f||m|}\right)^{1/2}. \tag{4.2}$$

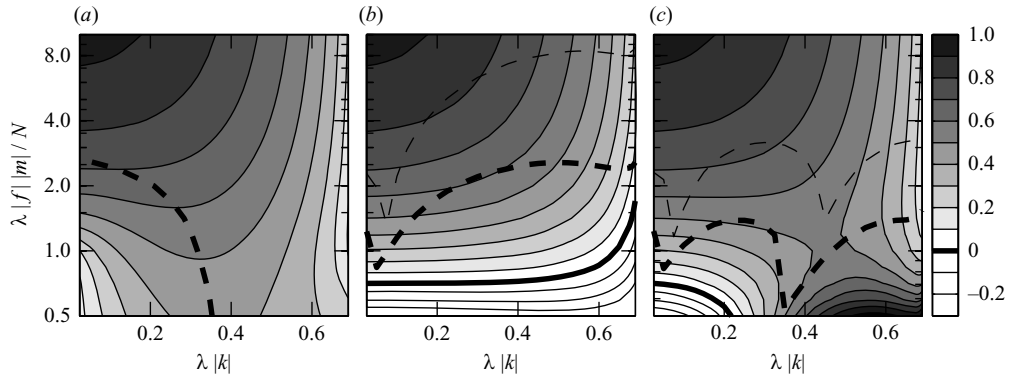

FIGURE 5. (a) Numerically determined growth rate σ for the inertial instability of the flow (2.21) at $Ro = 2$. (*b*) The theoretical prediction $\sigma_{[1]}$. (*c*) The theoretical prediction $\sigma_{[2]}$. In each panel, the growth rate has been non-dimensionalized by $|f|$, the theoretical maximum at $Ro = 2$, and results are shown for $0.025 \leqslant \lambda|k| \leqslant 0.69$. In (*a*), the thick dashed line denotes the value of $|k|$ at which maximum growth rate is attained at fixed $|m|$. In (*b*) and (*c*) the thick dashed line marks where $|\sigma - \sigma_{[j]}| = 0.05|f|$, whilst the thin dashed line marks where $|\sigma - \sigma_{[j]}| = 0.005|f|$.

For physically meaningful solutions, (3.18) and (3.22) must also be satisfied. The latter is automatically satisfied, since $\overline{y}_k \to \overline{y} = 0$ as $k \to 0$, whilst the former requires

$$\lambda|k| < Ro^{-1/2}, \tag{4.3}$$

consistent with the scaling (3.10). Then using (3.19*b*) for ω_1 and (A13) for ω_2, for the $n = 0$ eigenmode, (3.13) gives

$$\omega \sim \pm f(1-Ro)^{1/2}\left(\left[1 - Ro\lambda^2k^2\right]^{1/2} + \frac{Ro^{1/2}|1-\lambda^2k^2|}{2(1-Ro)}\frac{m_f}{|m|} + \frac{(1-\lambda^2k^2)(Ro-2+9Ro\lambda^2k^2-8Ro^2\lambda^4k^4)}{8(1-Ro)^2(1-Ro\lambda^2k^2)^{3/2}}\frac{m_f^2}{m^2} + \ldots\right), \tag{4.4}$$

as $\tilde{m} \to \infty$, where $m_f = (N/|f|)\lambda^{-1}$ and $\lambda|k| < Ro^{-1/2}$. When $k = 0$, (4.4) reduces to (2.25). When $k \neq 0$, we anticipate a breakdown in the theory when $Ro \to 1$ or as $\lambda|k| \to Ro^{-1/2}$, for then the first two terms in the series become comparable.

4.2. *Numerical results*

We evaluate the accuracy of (4.4) by solving the eigenvalue problem numerically. Since (4.4) describes a single branch of the dispersion relation, we must compare it with the corresponding single branch of the numerically determined $\omega(k, m)$. Thus, rather than solving for the most unstable eigenmode, we seek the extension to finite k and $|m|$ of the $n = 0$ eigenmode obtained as $k \to 0$ and $|m| \to \infty$, as described in Appendix B.

Figure 5(*a*), shows the growth rate obtained from such an approach, at $Ro = 2$. The growth rate is symmetric about $k = 0$. At $k = 0$, the maximum growth rate is $|f|$, and from (2.23) the symmetric buoyancy cutoff is at $|m| = (N/|f|)\lambda^{-1}$. At large $|m|$, the growth rate decreases from $|f|$ as $|k|$ increases from zero, as expected from (3.5). However, for $|m| \lesssim 2.5(N/|f|)\lambda^{-1}$, the growth rate increases as $|k|$ increases from zero. Thus, for sufficiently small $|m|$, weak along-stream asymmetries destabilize the flow. When $k \neq 0$, there is no longer a buoyancy cutoff wavenumber m_b; rather, the growth

rate remains positive as $|m|$ decreases. Results from smaller $|m|$ (not shown), indicate that as $|m| \to 0$ the growth rate approaches that of the classical Kelvin–Helmholtz instability, with a maximum of $0.38|f|$. Thus, it appears that the inertial instability (at large $|m|$ and small k) is one and the same mode as the Kelvin–Helmholtz instability (at $m = 0$).

Figures 5(b) and (c) show the theoretical predictions $\sigma_{[1]}$ and $\sigma_{[2]}$ for the growth rate, determined from (3.24) and (4.4). It is clear that these recover the correct behaviour as $|m| \to \infty$, and that $\sigma_{[2]}$ is somewhat more accurate than $\sigma_{[1]}$. Note that $\sigma_{[2]}$ is accurate to within $0.15\,|f|$ when $|m| > (N/|f|)\lambda^{-1}$, so that once again, the results are useful when the scale separation condition (2.19) is violated. For yet smaller $|m|$, $\sigma_{[1]}$ and $\sigma_{[2]}$ become useless, and a Padé resummation of the series must be considered.

A striking feature of the numerical results is that $\mathrm{Re}(\omega)$ is apparently zero, presumably due to the symmetry of f and U in y. For all calculations, $|\mathrm{Re}(\omega)|$ has a maximum value of $3 \times 10^{-6}|f|$ and an average value of $3 \times 10^{-8}|f|$. This is consistent with (4.4), which implies $\mathrm{Re}(\omega) = 0$ when $Ro > 1$. Given that $\mathrm{Re}(\omega) = 0$, and normalizing the eigenmodes so that $\tilde{V}(0) = 1$, it follows that $\mathrm{Re}(\tilde{V})$ and $\mathrm{Im}(\tilde{V})$ are necessarily even and odd, respectively. This was apparent in figure 3(b), where $\tilde{V}(y)$ was shown at $k = 0.2\lambda^{-1}$ and $|m| = 8(N/|f|)\lambda^{-1}$. Also shown there is the corresponding theoretical prediction $\tilde{V}_{[0]}$, which satisfies $|\tilde{V}_{[0]} - \tilde{V}| < 0.12$. However, accuracy is lost for larger k or smaller $|m|$, and $\tilde{V}_{[1]}$ and $\tilde{V}_{[2]}$ give no improvement. Despite this failure, the growth rate is still predicted to high accuracy.

5. Instability of a uniform shear flow at the equator

Several previous theoretical studies (e.g. Boyd & Christidis 1982; Dunkerton 1983, 1993; Clark & Haynes 1996) have considered the stability of a zonal flow $U = U_0 + \Lambda y$ on an equatorial β-plane. When $m = 0$, the flow is stable, since $Q = \beta y - \Lambda$ implies that $\mathrm{d}Q/\mathrm{d}y$ is one-signed. However, as $|m|$ increases from zero, there is a weak instability at non-zero k associated with a critical-layer effect (Natarov & Boyd 2001). In contrast, when $k = 0$, there is an inertial instability when $|m| > m_b = 4N\beta/\Lambda^2$ (Dunkerton 1981). The instability is concentrated where $fQ < 0$, i.e. between $y = 0$ and $y = \Lambda/\beta$, and is centred at $\overline{y} = \Lambda/2\beta$. The inertial instabilities are strong, since the maximum possible growth rate implied by (1.6) of $|\Lambda|/2$ is achieved at $k = 0$ and as $|m| \to \infty$.

5.1. *Limiting solutions*

We apply the results of § 3.3 to this flow, recovering and extending the analysis of Clark & Haynes (1996). Equations (3.16a,b) lead to

$$\omega_0 = \pm\frac{\mathrm{i}\Lambda}{2}\left(1 - \frac{k^2\Lambda^2}{\beta^2}\right)^{-1/2}, \quad \overline{y}_k = \frac{\Lambda}{2\beta}\left(1 \mp \frac{\mathrm{i}k\Lambda}{\beta}\left(1 - \frac{k^2\Lambda^2}{\beta^2}\right)^{-1/2}\right), \tag{5.1}$$

and then (3.11b) and (3.17) give

$$L_k = \left(1 - \frac{k^2\Lambda^2}{\beta^2}\right)^{-1/4}\left(\frac{N}{\beta|m|}\right)^{1/2}, \quad a_k = \frac{\beta}{N}\left(1 - \frac{k^2\Lambda^2}{\beta^2}\right)^{1/2}. \tag{5.2}$$

These modes satisfy (3.22), and the condition (3.18) becomes $|k\Lambda/\beta| < 1$, consistent with the scaling (3.10). Then using (3.19b) for ω_1 and (A14) for ω_2, (3.13) and (3.23)

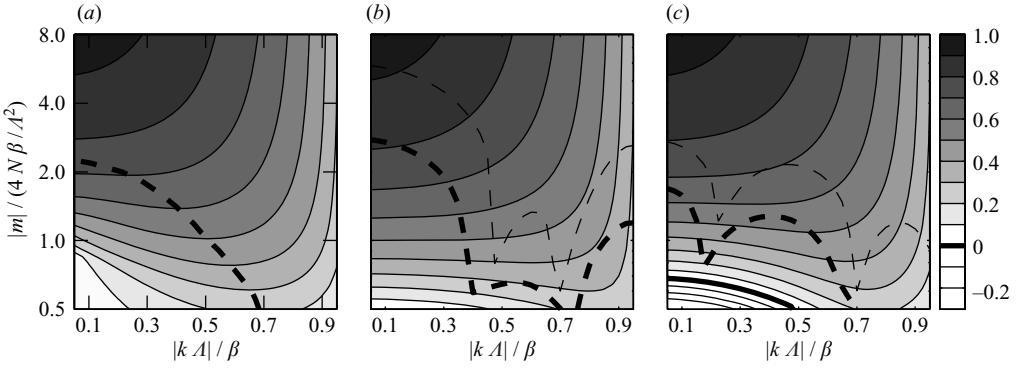

FIGURE 6. (*a*) Numerically determined growth rate σ for the inertial instability of a uniform shear flow on the equatorial β-plane. The thick dashed line denotes the value of $|k|$ at which maximum growth rate is attained at fixed $|m|$. (*b*) The theoretical prediction $\sigma_{[1]}$. (*c*) The theoretical prediction $\sigma_{[2]}$. In each panel, the growth rate has been non-dimensionalized by $|\Lambda|/2$, the theoretical maximum. In (*b*) and (*c*) the thin dashed line marks where $|\sigma - \sigma_{[j]}| = 0.002|\Lambda|$, whilst the thick dashed line marks where $|\sigma - \sigma_{[j]}| = 0.01|\Lambda|$.

give

$$\sigma \sim \pm\frac{\Lambda}{2}\left(1-\frac{k^2\Lambda^2}{\beta^2}\right)^{1/2} \times\left(1-\frac{2N\beta}{|m|\Lambda^2}\left(1-\frac{k^2\Lambda^2}{\beta^2}\right)^{1/2}-\frac{2N^2\beta^2}{m^2\Lambda^4}\left(1-\frac{2k^2\Lambda^2}{\beta^2}\right)^2+\ldots\right), \tag{5.3}$$

$$c \sim -\frac{2\beta N^2}{m^2\Lambda^2}\left(1-\frac{k^2\Lambda^2}{\beta^2}\right)\left(1-\frac{2k^2\Lambda^2}{\beta^2}\right)+\ldots, \tag{5.4}$$

as $|m| \to \infty$, for the $n = 0$ eigenmode. Elements of (5.3) have been developed previously: Winter & Schmitz (1998) gave the leading-order term, whilst Clark & Haynes (1996) gave the first two terms. Dunkerton (1993) gave a cubic equation yielding approximate solutions for ω, which would probably yield similar expressions as $|m| \to \infty$.

5.2. *Numerical results*

We evaluate the accuracy of (5.3) and (5.4) by solving the eigenvalue problem numerically. As in §4.2, we solve for the extension to finite k and $|m|$ of the $n = 0$ eigenmode obtained as $k \to 0$ and $|m| \to \infty$. Numerical details are given in Appendix B. As noted by Dunkerton (1983), solutions only exist when $|k\Lambda/\beta| < 1$, as may be diagnosed by consideration of (1.3) as $|y| \to \infty$, so attention is confined to this region. Apparently by chance, this is equivalent to the condition for the existence of localized solutions.

The numerically determined growth rate is shown in figure 6(*a*) (cf. figure 1 of Dunkerton 1993). At $k = 0$, the growth rate approaches $|\Lambda|/2$ as $|m| \to \infty$, but falls to zero at $m_b = 4N\beta/\Lambda^2$. At large $|m|$, the growth rate decreases as $|k|$ increases from zero, consistent with (3.4). However, for sufficiently small $|m|$, the growth rate increases as $|k|$ increases from zero, the transition occurring at $|m| = 2.24\,m_b$ (Clark & Haynes 1996). Figures 6(*b*) and (*c*) show the theoretical predictions $\sigma_{[1]}$ and $\sigma_{[2]}$ for the growth rate, determined from (3.24) and (5.3). Note that $|\sigma_{[2]} - \sigma| < 0.002\,|\Lambda|$ when $|m| > 2\,m_b$, whilst $|\sigma_{[2]} - \sigma| < 0.01\,|\Lambda|$ when $|m| > 0.5\,m_b$ and $|k| > 0.7|\Lambda|/\beta$.

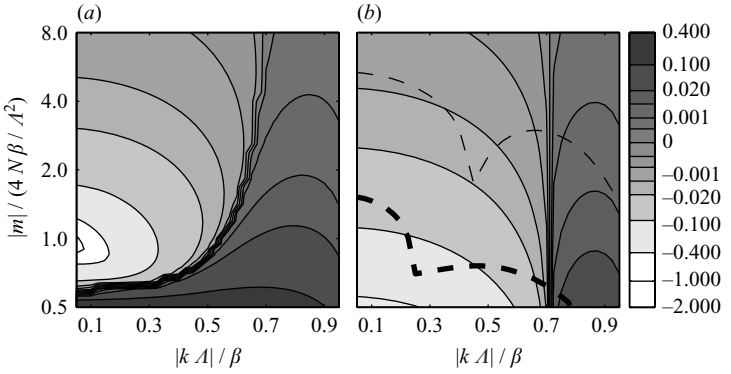

FIGURE 7. (*a*) Numerically determined intrinsic phase speed c for the inertial instability of a uniform shear flow on the equatorial β-plane. (*b*) The theoretical prediction $c_{[2]}$. In each panel, c has been non-dimensionalized by Λ^2/β. In (*b*), the thin dashed line marks where $|c - c_{[2]}| = 0.001\Lambda^2/\beta$, whilst the thick dashed line marks where $|c - c_{[2]}| = 0.1\Lambda^2/\beta$.

The prediction $\sigma_{[1]}$ is somewhat less accurate. Both predictions can be significantly improved as $k \to 0$ by using expressions for σ^2 rather than σ, since in that limit there exists an exact expression for σ^2.

The numerically determined intrinsic phase speed c is shown in figure 7(*a*). As $|m| \to \infty$, $c \to 0$ for all $|k|$. The largest absolute values occur near $|m| = m_b$ and $k = 0$, where c falls to $-1.6\Lambda^2/\beta$. The theoretical prediction $c_{[2]}$, determined from (5.4), is shown in figure 7(*b*). We can see that $c_{[2]} \to c$ as $|m| \to \infty$, so that $c \sim |m|^{-2}$ in this limit. The expression $c_{[2]}$ is accurate to within $0.1\Lambda^2/\beta$ for most of the values shown. Relatively large errors are expected when $|m| \sim 4N\beta/\Lambda^2$, since we have only derived the leading-order term of the series for c.

The latitudinal structure $\tilde{V}(y)$ of the $n = 0$ eigenmode at $k = 0.5\beta/\Lambda$ is shown in figure 8, where $\Lambda > 0$. At both $|m| = 8m_b$ and $|m| = m_b$, $\tilde{V}(y)$ takes the form of oscillations modulated by a Gaussian envelope. This is consistent with the theoretical predictions, the leading-order terms of which can be derived from (3.19*a*). Renormalizing so that $\tilde{V} = 1$ at $y = \overline{y}$, we obtain:

$$\tilde{V} \sim \exp\left(\mathrm{i}l\,(y - \Lambda/2\beta)\right) \exp\left(-\frac{(y - \Lambda/2\beta)^2}{2L_k^2}\right), \quad l = \mp\frac{\Lambda^2 k|m|}{2N\beta}, \tag{5.5}$$

with the minus sign corresponding to the unstable eigenmode. Thus, the cross-stream structure is characterized by decay on a length scale L_k, given by (5.2), and by oscillations with wavenumber l. At fixed $|m|$, as $|k|$ increases, the width of the envelope increases and the wavelength of the oscillations decreases, so the oscillations become more apparent. At fixed k, as $|m|$ decreases, the width of the envelope increases as $|m|^{-1/2}$ whilst the wavelength of the oscillations increases as $|m|^{-1}$, so the oscillations become less apparent. Thus, at $|m| = m_b$ in figure 8(*b*), $\mathrm{Re}(\tilde{V})$ looks rather like a Gaussian, and $\mathrm{Im}(\tilde{V})$ is relatively small.

The theoretical prediction (5.5), along with higher-order predictions derived from (A10) and (A11), are also shown in figure 8. At $|m| = 8m_b$ and $k = 0.5\beta/\Lambda$, $\tilde{V}_{[0]}$ offers an adequate approximation, whilst differences between $\tilde{V}$ and $\tilde{V}_{[2]}$ are barely perceptible, with $|\tilde{V} - \tilde{V}_{[2]}| < 0.013$. At $|m| = m_b$ and $k = 0.5\beta/\Lambda$, $\tilde{V}_{[0]}$ is no longer a good approximation, but $\tilde{V}_{[2]}$ is still qualitatively and quantitatively correct, with $|\tilde{V} - \tilde{V}_{[2]}| < 0.2$. The accuracy of $\tilde{V}_{[0]}$, $\tilde{V}_{[1]}$ and $\tilde{V}_{[2]}$ over a wide parameter regime is

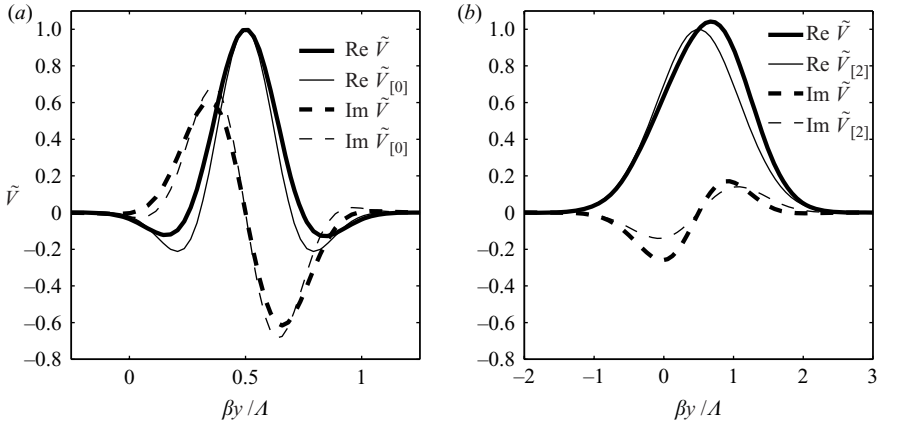

FIGURE 8. The latitudinal structure at $k = 0.5\,\beta/\Lambda$ and (*a*) $|m| = 8m_b$, (*b*) $|m| = m_b$.

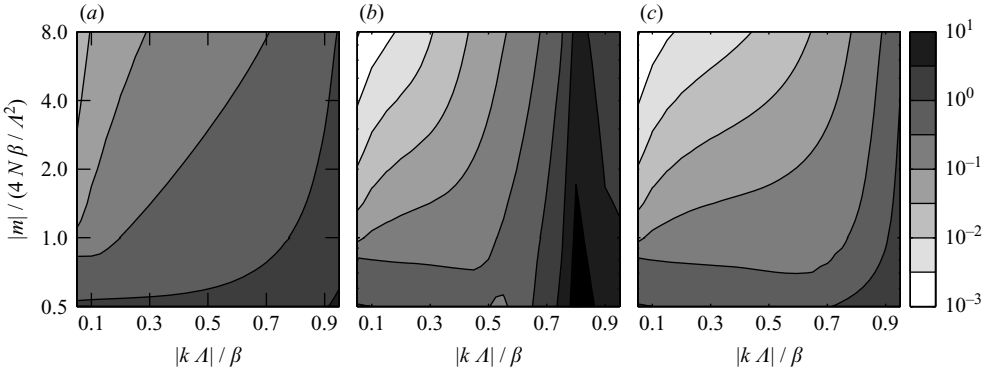

FIGURE 9. Accuracy of the predicted latitudinal structure: (*a*) $\max|\tilde{V} - \tilde{V}_{[0]}|$, (*b*) $\max|\tilde{V} - \tilde{V}_{[1]}|$, (*c*) $\max|\tilde{V} - \tilde{V}_{[2]}|$. The eigenmodes are normalized so that $\tilde{V} = 1$ at $y = \Lambda/2\beta$.

shown in figure 9. The accuracy of each typically increases as k decreases and $|m|$ increases. This is to be expected, since from (5.2) the latitudinal scale of the eigenmodes L_k becomes smaller in these limits, so that the scale separation underlying the analysis becomes greater. The scale separation is always lost as $|k\Lambda/\beta| \to 1$ or as $|m| \to 0$, since then $L_k \to \infty$. As shown in figure 9(*c*), $\tilde{V}_{[2]}$ is a useful approximation for a wide range of k and $|m|$.

5.3. *Applications to the equatorial stratosphere and mesosphere*

The upper stratosphere and lower mesosphere have a persistent cross-equatorial shear near-solstice, which could be crudely modelled as a zonally symmetric flow with uniform shear. The structure of the zonally symmetric instability is well known (e.g. Dunkerton 1981), whilst the horizontal structure of zonally non-symmetric disturbances has been illustrated by Dunkerton (1983, 1993), Winter & Schmitz (1998), and Taniguchi & Ishiwatari (2006). However, since observations of inertial instability in the equatorial stratosphere are perhaps most compelling when shown as meridional slices of temperature perturbations (e.g. figure 5*b* of Hayashi *et al.* 1998), and since temperature perturbations have the same structure as the vertical gradient of the geopotential perturbation $\tilde{\phi}$, we examine the meridional structure of $\tilde{\phi}$.

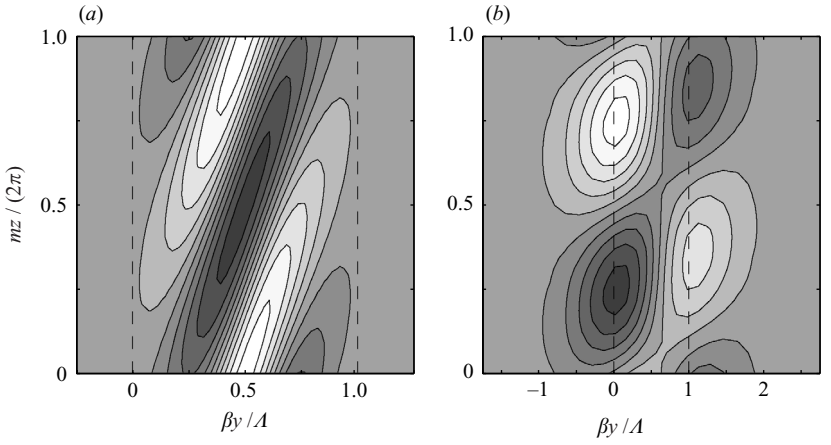

FIGURE 10. Numerically determined $\tilde{\phi}$, at fixed x. Parameters are (*a*) $k = 0.5\,\beta/\Lambda$, $|m| = 8m_b$; (*b*) $k = 0.5\,\beta/\Lambda$, $|m| = m_b$. The vertical dashed lines denote the edge of the unstable region.

Figure 10 shows numerically determined $\tilde{\phi}$ at $k = 0.5\beta/\Lambda$, corresponding to the two cases shown in figure 8. Figure 10(*a*), at $|m| = 8m_b$, shows the form of $\tilde{\phi}$ at relatively large vertical wavenumber. This is in marked contrast to the classical picture of inertial instability based on zonally symmetric theory, i.e. opposite-signed temperature perturbations approximately equidistant from the centre of the unstable region. However, structures with such large vertical wavenumbers may not be realized in the atmosphere, because the vertical scale of the instability is likely to be limited by diffusion (Dunkerton 1981) or a nonlinear mechanism (Griffiths 2003b). Then, zonally asymmetric inertial instabilities of moderate vertical scales are expected to be the dominant motions, as noted by Dunkerton (1983) and Stevens & Ciesielski (1986). Figure 10(*b*), at $|m| = m_b$, shows such a case. This is remarkably similar to the classical picture of inertial instability based on zonally symmetric theory. An important difference is the larger amplitude of the equatorial cells, which is perhaps suggestive of the Kelvin-wave instability which the inertial instability is set to merge with at yet smaller $|m|$ (Boyd & Christidis 1982). It is not clear whether this solution should be described as an inertial instability, or whether another interpretation might be more appropriate (Taniguchi & Ishiwatari 2006).

The non-symmetric solutions have a propagating character, since $\mathrm{Re}(\omega) \neq 0$. Taking $\beta = 2.3 \times 10^{-11}\mathrm{m}^{-1}\mathrm{s}^{-1}$ and $\Lambda = 4 \times 10^{-5}\,\mathrm{s}^{-1}$ (see § 2d of Griffiths 2003*b*), the requirement $k = j/r_e$ (where j is an integer and r_e is the Earth's radius) implies $|k\Lambda/\beta| = 0.27j$. From figure 7(*a*), $|c| \sim 0.2\Lambda^2/\beta \approx 14\,\mathrm{m\,s}^{-1}$ for such eigenmodes, with both positive and negative phase speeds possible. The corresponding values of $\mathrm{Re}(\omega)$ imply a negligible vertical phase speed. However, since $c \sim |m|^{-2}$ for this uniform shear flow, whereas we expect $c \sim |m|^{-1}$ for flows with non-uniform shear, it is possible that c will be larger for more realistic flows.

6. Discussion

The Rayleigh–Schrödinger perturbation analysis employed here is the natural choice for studying inertial instabilities. The underlying reason is that, when the along-stream wavenumber $k = 0$ and as the absolute value of the vertical wavenumber $|m| \to \infty$, inertial instabilities are highly localized on a length scale $\propto |m|^{-1/2}$ around the

streamline where fQ is minimized. This is an important limit, since it corresponds to the strongest linear instabilities when $k = 0$. It also has a clear dynamical interpretation, the motions becoming near-inertial as $|m| \to \infty$, with horizontal pressure gradients playing a negligible role. As $|m|$ is reduced, the inertial balance is broken by a stabilizing cross-stream pressure gradient associated with buoyancy, and for $|m| < m_b$, which takes the scaling (2.15), the solutions become inertia–gravity waves. However, for $|m| > m_b$ the traditional labelling of an inertial instability is justified because the instability originates in the near-inertial limit $|m| \to \infty$. Although not explicitly illustrated here, the cross-stream localization of the solutions renders the lateral boundary conditions rather unimportant, so that the limiting solution is identical for laterally bounded, unbounded, or periodic domains.

These ideas are well established. However, here it has been shown that a similar approach can be applied to the instability analysis with non-zero k, for an arbitrary parallel shear flow. Our results are thus similar in nature to those of Billant & Gallaire (2005), who applied a complex WKB method to the non-axisymmetric instability of flows with circular symmetry. In § 3.1, the general structure of the solutions was explicitly illustrated at small k and large $|m|$. In addition to the buoyancy-induced stabilization as $|m|$ decreases, there is a stabilization as $|k|$ increases from zero, again associated with growth of the cross-stream pressure gradient. For larger $|k|$, these localized solutions may cease to exist, with detailed examples showing that the analysis holds only when $0 \leqslant |k| < k_c$, with k_c taking the scaling (3.10). For sufficiently large $|m|$ and $0 \leqslant |k| < k_c$, it is justifiable to describe these localized solutions as inertial instabilities, or non-symmetric inertial instabilities, since they originate in the near-inertial limit $k \to 0$ and $|m| \to \infty$. There is a clear analogy here with the use of 'inertial instability' at $k = 0$ when $|m| > m_b$. This is also consistent with terminology used by Dunkerton (1983), and Stevens & Ciesielski (1986), for instance. However, when $k \neq 0$, as $|m|$ is reduced the growth rate typically remains positive, and as $|m| \to 0$ the solutions are clearly identifiable as something other than an inertial instability. Even though these solutions are smoothly connected to those obtained in the near-inertial limit, their description as inertial instabilities will generally be inappropriate for sufficiently small $|m|$. In our detailed examples, the inertial instability merges into a barotropic Kelvin–Helmholtz instability (see § 4) or a Kelvin-wave instability (see § 5) at small $|m|$. A similiar connection was noted by Sipp *et al.* (2005) for the instability of a vortex with radial stratification, where the inertial instability merges into an analogue of the Rayleigh–Taylor instability at small $|m|$.

Although the analysis only describes a certain discrete class of normal-mode solutions, these are of physical interest. For instance, on the equatorial β-plane, when $k = 0$ the discrete eigenmodes typically form a complete set, so that the dynamics of the linear initial-value problem are captured by the analysis, at least for disturbances of high vertical wavenumber. On the f-plane, typically the discrete spectrum is finite, so that the analysis only describes a finite number of eigenmodes. However, if the minimum value of fQ is negative but with fQ positive and finite as $|y| \to \infty$, corresponding to a region (or regions) prone to inertial instability within an otherwise stable flow, then the unstable solutions are necessarily part of the discrete spectrum (since $\omega^2 < 0$ and $fQ > 0$ as $|y| \to \infty$ imply exponentially decaying solutions, from (2.1)). Thus, the asymptotic analysis captures the normal mode instability. When $k \neq 0$, the situation is more complicated, as other branches of the dispersion relation not captured by the analysis also describe instabilities. However, the inertial instabilities obtained as $|m| \to \infty$ are typically strong, when measured relative to the maximum possible normal-mode growth rate (1.6).

A major benefit of the analysis is its simplicity. The first two terms of asymptotic expansions for the frequency ω, and the corresponding leading-order cross-stream structure, can be almost trivially determined. Of particular interest is the accuracy of the predictions for $\omega(k, m)$. For the most unstable solutions, which are obtained as $|m| \to \infty$, ω is approximated well, since in that limit the cross-stream scale separation underlying the analysis is valid. Both the first- and second-order expressions for ω remain useful as $|m|$ decreases, typically even when $|m| \approx m_b$, which is outside the range of validity which might otherwise be expected. Clark & Haynes (1996) have shown one way in which such analytical expressions for $\omega(k, m)$ might be applied, in their study of the absolute instability of a flow with weak along-stream variations.

An immediate generalization of these ideas, discussed briefly in § 2.1, is to flows for which $fQ > 0$ everywhere, in which case the analysis describes trapped near-inertial waves as $k \to 0$ and $|m| \to \infty$, and their extension to inertia–gravity waves at finite $|m|$. When $k = 0$, there are connections here to studies of trapped near-inertial waves in oceanic vortices (e.g. Kunze 1985; Llewellyn Smith 1999), and to the work of Plougonven & Zeitlin (2005) on the role of trapped modes in geostropic adjustment. When $k \neq 0$, there are connections to studies of three-dimensional near-inertial waves (e.g. Kloosterziel & Müller 1995; Young & Ben Jelloul 1997).

6.1. *Extensions to other models*

We have developed solutions for an inviscid hydrostatic flow with constant buoyancy frequency, under the traditional approximation. However, it is worth noting the effect of relaxing each of these assumptions.

(i) Although viscosity damps all instabilities in the limit $|m| \to \infty$, a weak viscosity ν can be added to the formulation. The spatial structure of the solutions remains unchanged, but the growth rate is maximized at finite $|m| \sim \nu^{-1/3}$ (Griffiths 2008).

(ii) Relatively minor modifications to the theory should permit treatment of background flows where U and N vary with y and z, since the z-variations will be small compared with those of the perturbations in the limit $|m| \to \infty$. A WKB formulation for this kind of configuration was given by Griffiths (2000, chap. 3).

(iii) Billant & Gallaire (2005) have demonstrated that inertial instabilities of flows with circular symmetry are insensitive to stratification at large vertical wavenumber. In the present context, the importance of stratification can be assessed by considering the normal modes of a non-hydrostatic Boussinesq flow. Then the time evolution of pressure is given by

$$\left(\frac{\partial}{\partial t} + U(y)\frac{\partial}{\partial x}\right)\tilde{\phi} + \frac{N^2 - (\omega - kU)^2}{m^2}\left(\frac{\partial u}{\partial x} + \frac{\partial v}{\partial y}\right) = 0.$$

Comparing with (1.1c), we see that non-hydrostatic results can be obtained from the present theory by replacing N^2 by $N^2 - (\omega - kU)^2$. Thus, in the asymptotics of §§ 2 and 3, we replace N^2 by $N^2 - \omega_0^2$ to leading order. In particular, (3.4) becomes

$$\omega \sim k\overline{U} \pm \left(\overline{fQ}\right)^{1/2}\left(1 + \frac{2n+1}{2|m|\overline{(fQ)}}\left(N^2 - \overline{fQ}\right)^{1/2}\left(\frac{\overline{(fQ)''}}{2}\right)^{1/2} - \frac{k^2\overline{U'}^2}{\overline{(fQ)''}} + \dots\right),$$

as $k \to 0$ and $|m| \to \infty$. Thus, even taking the extreme limit $N = 0$, when $\overline{fQ} < 0$ the inertial instabilities retain the same character as in the hydrostatic case, with the largest growth rates obtained as $|m| \to \infty$ and $k \to 0$. Stratification does influence the degree of stabilization as $|m|$ decreases, but it does not influence the stabilization as $|k|$ increases from zero. However, if $\overline{fQ} > N^2 > 0$, i.e. for a weakly stratified

and inertially stable flow, then the results must be modified since (2.4) implies that localized solutions only exist when $\overline{(fQ)}'' < 0$.

(iv) Although applying the hydrostatic approximation has a benign influence upon inertial instabilities, the neglect of the horizontal component of the Coriolis parameter in the formulation should be addressed. This leads to an important modification of the theory as $|m| \to \infty$, which will be discussed elsewhere.

Appendix A. Higher-order corrections

We start by noting some properties of the Hermite functions $H_n(Y)$:

$$\frac{\mathrm{d}H_n}{\mathrm{d}Y} = nH_{n-1} - \tfrac{1}{2}H_{n+1}, \qquad 2YH_n = 2nH_{n-1} + H_{n+1}, \tag{A1a,b}$$

which follow from (2.8). Repeatedly applying (A1b) implies that

$$4Y^2H_n = 4n(n-1)H_{n-2} + 2(2n+1)H_n + H_{n+2}, \tag{A1c}$$

$$8Y^3H_n = 8n(n-1)(n-2)H_{n-3} + 12n^2H_{n-1} + 6(n+1)H_{n+1} + H_{n+3}, \tag{A1d}$$

$$\begin{aligned} 16Y^4H_n = {} & 16n(n-1)(n-2)(n-3)H_{n-4} + 16n(n-1)(2n-1)H_{n-2} \\ & + 12(2n^2+2n+1)H_n + 4(2n+3)H_{n+2} + H_{n+4}. \end{aligned} \tag{A1e}$$

We also introduce a Hermite operator

$$\mathscr{L}_n = \frac{\mathrm{d}^2}{\mathrm{d}Y^2} + 2n + 1 - Y^2 \quad \Rightarrow \quad \mathscr{L}_n H_m(Y) = 2(n-m)H_m(Y). \tag{A2a,b}$$

A.1. *Symmetric solutions*

We calculate the next-order corrections to (2.17), subject to the normalization condition

$$\int_{-\infty}^{\infty} \tilde{V} H_n \,\mathrm{d}Y = \int_{-\infty}^{\infty} H_n^2 \,\mathrm{d}Y. \tag{A3}$$

Substituting (2.16a) into (2.6), we obtain

$$\mathscr{L}_n \tilde{V} = \left(\frac{L\overline{(fQ)}'''Y^3}{6a^2N^2} + \frac{L^2\overline{(fQ)}''''Y^4}{24a^2N^2} + \ldots - \frac{a^2L^2\omega_2^2}{N^2} - \frac{a^4L^4\omega_3^2}{N^2} - \ldots \right) \tilde{V}, \tag{A4}$$

using (2.17) and (A2a). Substituting from (2.16b), the leading-order terms of (A4) are satisfied by $\tilde{V}_0 = H_n(Y)$, applying (A3). The $O(L)$ terms of (A4) then give

$$\mathscr{L}_n \tilde{V}_1 = \frac{\overline{(fQ)}'''}{6a^3N^2} Y^3 H_n.$$

Thus, using (A1d), (A2b) and (A3) we can show that

$$\tilde{V}_1 = \frac{\overline{(fQ)}'''}{6a^3N^2} \left(\tfrac{1}{6}n(n-1)(n-2)H_{n-3} + \tfrac{3}{4}n^2H_{n-1} - \tfrac{3}{8}(n+1)H_{n+1} - \tfrac{1}{48}H_{n+3} \right). \tag{A5}$$

The $O(L^2)$ terms of (A4) then give

$$\mathscr{L}_n \tilde{V}_2 = \frac{\overline{(fQ)}'''}{6a^3N^2} Y^3 \tilde{V}_1 + \frac{\overline{(fQ)}''''}{24a^4N^2} Y^4 H_n(Y) - \frac{\omega_2^2}{N^2} H_n(Y).$$

Multiplying by H_n and integrating with respect to Y from $-\infty$ to ∞, the left-hand side vanishes, and we find that the right-hand side cannot project onto H_n. Thus,

using (A1*d*,*e*) and (A5), and substituting for a from (2.5*b*), we can extract a solvability condition:

$$\omega_2^2 = \frac{N^4}{8\overline{(fQ)''}}\left((2n^2+2n+1)\frac{\overline{(fQ)''''}}{\overline{(fQ)''}} - \frac{(30n^2+30n+11)}{9}\left(\frac{\overline{(fQ)''}}{\overline{(fQ)''}}\right)^2\right). \tag{A6}$$

A.2. *Non-symmetric solutions*

We calculate the higher-order behaviour of $\tilde{V}(y)$ and ω for the $n=0$ eigenmode, with $k \neq 0$. We return to (3.12), but include terms up to $O(L_k^4)$. We thus must extend (3.15), noting that the $O(1)$ and $O(L_k)$ terms vanish using (3.16*a*,*b*), and that the $O(L_k^2)$ terms can be simplified using (3.17) and (3.19*b*). We obtain

$$\frac{\hat{\omega}^2 - fQ}{N^2} = (a_k L_k)^2\left(2n+1-Y^2\right) - (a_k L_k)^3\left(\gamma_3 Y^3 + \frac{(2n+1)k\overline{U_k'}Y}{a_k\omega_0}\right) - (a_k L_k)^4 \times\left(\gamma_4 Y^4 + \frac{(2n+1)k\overline{U_k''}Y^2}{2\omega_0 a_k^2} - \frac{2\omega_0\omega_2}{N^2} - \frac{(2n+1)^2N^2}{4\omega_0^2}\right) + O(L_k^5), \tag{A7}$$

where the dimensionless coefficients γ_3 and γ_4 are given by

$$\gamma_3 = \frac{1}{N^2 a_k^3}\left(\tfrac{1}{6}\overline{(fQ)'''_k} + \tfrac{1}{3}k\omega_0\overline{U_k'''} - k^2\overline{U'U_k''}\right), \tag{A8a}$$

$$\gamma_4 = \frac{1}{N^2 a_k^4}\left(\tfrac{1}{24}\overline{(fQ)''''_k} + \tfrac{1}{12}k\omega_0\overline{U_k''''} - \tfrac{1}{3}k^2\overline{U'U_k'''} - \tfrac{1}{4}k^2\overline{U_k''^2}\right). \tag{A8b}$$

Substituting into (3.12), the equation for the $n=0$ eigenmode becomes

$$\mathscr{L}_0\tilde{V} = a_k L_k\left[\gamma_3 Y^3 + \frac{k\overline{U_k'}}{a_k\omega_0}\left(Y - 2\frac{\mathrm{d}}{\mathrm{d}Y}\right)\right]\tilde{V} - 2(a_k L_k)^2\left[\frac{k^2\overline{U_k'^2}}{\omega_0^2 a_k^2} + \frac{k\overline{U_k''}}{\omega_0 a_k^2}\right] Y\frac{\mathrm{d}\tilde{V}}{\mathrm{d}Y} + (a_k L_k)^2\left[\gamma_4 Y^4 + \frac{k\overline{U_k''}Y^2}{2\omega_0 a_k^2} - \frac{2\omega_0\omega_2}{N^2} - \frac{N^2}{4\omega_0^2} + \frac{1}{a_k^2}\left(k^2 + \frac{k\overline{Q_k'}}{\omega_0} + \frac{2k^2\overline{QU_k'}}{\omega_0^2}\right)\right]\tilde{V} + O(L_k^3). \tag{A9}$$

We choose to apply (A3), so that the leading-order terms of (A9) yield $\tilde{V}_0 = H_0(Y) = \exp(-Y^2/2)$. Expanding $\tilde{V}$ according to (3.14), the $O(L_k)$ terms of (A9) then give

$$\mathscr{L}_0\tilde{V}_1 = \left(\gamma_3 Y^3 + \frac{3kY\overline{U_k'}}{a_k\omega_0}\right) H_0(Y).$$

Thus, using (A1*b*,*d*), (A2*b*) and (A3), we can show that

$$\tilde{V}_1 = -\frac{3k\overline{U_k'}}{4a_k\omega_0}H_1(Y) - \frac{\gamma_3}{48}\left[18H_1(Y) + H_3(Y)\right]. \tag{A10}$$

The $O(L_k^2)$ terms of (A9) then give

$$\mathscr{L}_0\tilde{V}_2 = \left[\gamma_3 Y^3 + \frac{k\overline{U_k'}}{a_k\omega_0}\left(Y - 2\frac{\mathrm{d}}{\mathrm{d}Y}\right)\right]\tilde{V}_1 + \frac{2}{a_k^2}\left(\frac{k^2\overline{U_k'^2}}{\omega_0^2} + \frac{k\overline{U_k''}}{\omega_0}\right) Y^2 H_0(Y) + \left[\gamma_4 Y^4 + \frac{k\overline{U_k''}Y^2}{2\omega_0 a_k^2} - \frac{2\omega_0\omega_2}{N^2} - \frac{N^2}{4\omega_0^2} + \frac{1}{a_k^2}\left(k^2 + \frac{k\overline{Q_k'}}{\omega_0} + \frac{2k^2\overline{QU_k'}}{\omega_0^2}\right)\right] H_0(Y). \tag{A11}$$

Since the right-hand side cannot project onto H_0, using (A1*a–e*) we find that

$$\omega_2 = \frac{N^2}{2\omega_0}\left(\frac{1}{a_k^2}\left[k^2 + \frac{k\overline{Q_k'}}{\omega_0} + \frac{5k\overline{U_k''}}{4\omega_0} + \frac{2k^2\overline{QU_k'}}{\omega_0^2} + \frac{7k^2\overline{U_k'^2}}{4\omega_0^2}\right] + \frac{3\gamma_4}{4} - \frac{11\gamma_3^2}{16} - \frac{3k\overline{U_k'}\gamma_3}{4a_k\omega_0} - \frac{N^2}{4\omega_0^2}\right), \tag{A12}$$

where γ_3 and γ_4 are given by (A8*a*,*b*).

For the flow of § 4, we can show using (4.1) and (4.2) that

$$\gamma_3 = \frac{2Nk\lambda\omega_0}{f|f|}\frac{(Ro^{-1} - k^2\lambda^2)^{1/2}}{|1 - k^2\lambda^2|}, \quad \gamma_4 = \frac{N^2}{3f^2Ro}\frac{\left((9 - 7Ro)\,k^2\lambda^2 - 2\right)}{\left(1 - k^2\lambda^2\right)^2},$$

so that (A12) gives

$$\omega_2 = \frac{N^4}{8\omega_0 f^2}\left(\frac{Ro - 2 + 9Ro\lambda^2k^2 - 8Ro^2\lambda^4k^4}{Ro(1 - Ro)(1 - \lambda^2k^2)}\right). \tag{A13}$$

For the flow of § 5, it is easy to see that $\gamma_3 = \gamma_4 = 0$, so that (5.1), (5.2) and (A12) give

$$\omega_2 = \mp\frac{\mathrm{i}N^4}{\Lambda^3\left(1 - k^2\Lambda^2/\beta^2\right)^{1/2}}\left(1 - \frac{2k^2\Lambda^2}{\beta^2}\right)^2 - \frac{2kN^4}{\beta\Lambda^2}\left(1 - \frac{2k^2\Lambda^2}{\beta^2}\right). \tag{A14}$$

Appendix B. Numerical methods

Eigenvalue problems on $-\infty < y < \infty$ are solved by mapping to a finite numerical domain $-1 \leqslant \eta \leqslant 1$, via

$$\eta = \frac{y - y_c}{\sqrt{(y - y_c)^2 + \lambda_c^2}}, \tag{B1}$$

where y_c and λ_c are free parameters. We then discretize on a uniform grid $\eta_j = -1 + (2j - 1)/2J$, $j = 1, 2, \ldots, J$, and apply the periodic pseudospectral method with differentiation matrices derived as in Fornberg (1998, pp. 31–34). The boundary conditions (1.5) need not be imposed explicitly, as described by Boyd (2000, § 17.8).

When $k = 0$, we apply this approach to (2.1), which then reduces to a $J \times J$ matrix eigenvalue problem for ω^2. We solve for the smallest value of ω^2 at $J = 32$, using an iterative solver, and double J until ω^2 changes by less than a specified tolerance. The results of § 2.5 were obtained with $y_c = \overline{y}$ and $\lambda_c = 2L$, with ω^2 calculated to within $10^{-6} \times \Lambda^2/4$, which typically required $J = 128$.

When $k \neq 0$, we apply a corresponding approach by writing each of $\tilde{U}(y)$, $\tilde{V}(y)$ and $\tilde{\Phi}(y)$ as a J-component vector, so that (1.1*a–c*) reduces to a $3J \times 3J$ matrix eigenvalue problem for ω. Rather than simply solve for the most unstable eigenmode, we instead seek the extension to finite k and $|m|$ of the inertial instability obtained as $k \to 0$ and $|m| \to \infty$. To do this, we first solve for the eigenvalue with largest $\mathrm{Im}(\omega)$ at $k = 0$ and large $|m|$, which corresponds to the $n = 0$ eigenmode. We then solve for ω at $k + \Delta k$, using an iterative eigenvalue solver with initial guess $\omega(k)$, and repeat to track ω for this eigenmode up to some maximum k. Then, at each k, we solve for ω at $m - \Delta m$, initializing with $\omega(k, m)$, and repeat to track ω down to some minimum m. Provided Δk and Δm are sufficiently small, we do not jump between different branches of $\omega(k, m)$.

For the results of §4, we used (B1) with $y_c = 0$ and $\lambda_c = \min(4L, 4\lambda)$. For each solution, J was doubled until ω changed by less than $2 \times 10^{-4}|f|$, although typically, convergence occurred to a much higher precision after just the first iteration from $J = 32$ to $J = 64$. An exception occurred as $\lambda|k| \to Ro^{-1/2} = 2^{-1/2}$, when the growth rate tends to zero and the solution becomes highly oscillatory, requiring $J = 1024$ at $|m| = 10(N/|f|)\lambda^{-1}$ and $k = 0.69\lambda^{-1}$. Clearly, some kind of transition in the solution is being approached, consistent with the prediction of (4.3) for the existence of localized solutions. Solutions were not found for $|k| > 0.69\lambda^{-1}$.

For the results of §5, we used (B1) with $y_c = \Lambda/2\beta$, $\lambda_c = 4L_k$, and calculated ω to within an accuracy of $10^{-4} \times \Lambda$. For most parameters this required $J = 64$, but for some points near $k = 0.95\Lambda/\beta$ and $|m| = 32N\beta/\Lambda^2$, convergence was reached only at $J = 256$. Near to $|m| = m_b$ for small k, considerable care must be taken to avoid jumping between different branches of the dispersion relation, owing to the merging of roots discussed by Boyd & Christidis (1982). At the lowest value of k used ($k = 0.05\beta/\Lambda$), increments of $\Delta m = 0.2N\beta/\Lambda^2$ were used for $2N\beta/\Lambda^2 < |m| < 4N\beta/\Lambda^2$.

REFERENCES

Andrews, D. G., Holton, J. R. & Leovy, C. B. 1987 *Middle Atmosphere Dynamics*. Academic.

Bayly, B. J. 1988 Three dimensional centrifugal-type instabilities in inviscid two-dimensional flows. *Phys. Fluids* **31**, 56–64.

Bender, C. M. & Bettencourt, L. M. A. 1996 Multiple-scale analysis of quantum systems. *Phys. Rev.* D **54**, 7710–7723.

Bender, C. M. & Orszag, S. A. 1978 *Advanced Mathematical Methods for Scientists and Engineers*. McGraw-Hill.

Billant, P. & Gallaire, F. 2005 Generalized Rayleigh criterion for non-axisymmetric centrifugal instabilities. *J. Fluid Mech.* **542**, 365–379.

Boyd, J. P. 1978 The effects of latitudinal shear on equatorial waves. Part I: Theory and methods. *J. Atmos. Sci.* **35**, 2236–2258.

Boyd, J. P. 2000 *Chebyshev and Fourier Spectral Methods*. Dover.

Boyd, J. P. & Christidis, Z. D. 1982 Low wavenumber instability on the equatorial beta-plane. *Geophys. Res. Lett.* **9**, 769–772.

Chomaz, J., Huerre, P. & Redekopp, L. G. 1991 A frequency selection criterion in spatially developing flows. *Stud. Appl. Maths.* **84**, 119–144.

Clark, P. D. & Haynes, P. H. 1996 Inertial instability on an asymmetric low-latitude flow. *Q. J. R. Met. Soc.* **122**, 151–182.

Dunkerton, T. J. 1981 On the inertial stability of the equatorial middle atmosphere. *J. Atmos. Sci.* **38**, 2354–2364.

Dunkerton, T. J. 1983 A nonsymmetric equatorial inertial instability. *J. Atmos. Sci.* **40**, 807–813.

Dunkerton, T. J. 1993 Inertial instability of nonparallel flow on an equatorial beta plane. *J. Atmos. Sci.* **50**, 2744–2758.

Fornberg, B. 1998 *A Practical Guide to Pseudospectral Methods*. Cambridge University Press.

Griffiths, S. D. 2000 Inertial instability in the equatorial stratosphere. PhD thesis, University of Cambridge.

Griffiths, S. D. 2003*a* The nonlinear evolution of zonally symmetric equatorial inertial instability. *J. Fluid Mech.* **474**, 245–273.

Griffiths, S. D. 2003*b* Nonlinear vertical scale selection in equatorial inertial instability. *J. Atmos. Sci.* **60**, 977–990.

Griffiths, S. D. 2008 Weakly diffusive vertical scale selection for the inertial instability of an arbitrary shear flow. *J. Fluid Mech.* **594**, 265–268.

Hayashi, H., Shiotani, M. & Gille, J. C. 1998 Vertically stacked temperature disturbances near the equatorial stratopause as seen in cryogenic limb array etalon spectrometer data. *J. Geophys. Res.* **103**, 19469–19483.

Holton, J. R. 1992 *An Introduction to Dynamic Meteorology*, 3rd edn. Academic.

Killworth, P. D. 1980 Barotropic and baroclinic instability in rotating stratified fluids. *Dyn. Atmos. Oceans* **4**, 143–184.

Kloosterziel, R. C. & Müller, P. 1995 Evolution of near-inertial waves. *J. Fluid Mech.* **301**, 269–294.

Knox, J. A. 2003 Inertial instability. In *Encyclopedia of Atmospheric Sciences* (ed. J. R. Holton, J. A. Curry & J. A. Pyle) pp. 1004–1013. Academic.

Kunze, E. 1985 Near-inertial wave propagation in geostrophic shear. *J. Phys. Oceanogr.* **15**, 544–565.

Leblanc, S. & Cambon, C. 1997 On the three-dimensional instabilities of plane flows subjected to Coriolis force. *Phys. Fluids* **9**, 1307–1316.

Llewellyn Smith, S. G. 1999 Near-inertial oscillations of a barotropic vortex: trapped modes and time evolution. *J. Phys. Oceanogr.* **29**, 747–761.

Messiah, A. 2000 *Quantum Mechanics*. Dover.

Michalke, A. 1964 On the inviscid instability of the hyperbolic-tangent velocity profile. *J. Fluid Mech.* **19**, 543–556.

Natarov, A. & Boyd, J. P. 2001 Beyond-all-orders instability in the equatorial Kelvin wave. *Dyn. Atmos. Oceans* **33**, 191–200.

d'Orgeville, M., Hua, B. L., Schopp, R. & Bunge, L. 2004 Extended deep equatorial layering as a possible imprint of inertial instability. *Geophys. Res. Lett.* **31**, L22303.

Plougonven, R. & Zeitlin, V. 2005 Lagrangian approach to geostrophic adjustment of frontal anomalies in a stratified fluid. *Geophys. Astrophys. Fluid Dyn.* **99**, 101–135.

Potylitsin, P. G. & Peltier, W. R. 1998 Stratification effects on the stability of columnar vortices on the *f*-plane. *J. Fluid Mech.* **335**, 45–79.

Richards, K. J. & Edwards, N. R. 2003 Lateral mixing in the equatorial Pacific: the importance of inertial instability. *Geophys. Res. Lett.* **30**, 1888.

Ripa, P. 1983 General stability conditions for zonal flows in a one-layer model on the β-plane or the sphere. *J. Fluid Mech.* **126**, 463–489.

Salmon, R. 1998 *Lectures on Geophysical Fluid Dynamics*. Oxford University Press.

Sergeev, A. V. & Goodson, D. Z. 1998 Summation of asymptotic expansions of multiple-valued functions using algebraic approximants: application to anharmonic oscillators. *J. Phys.* A **31**, 4301–4317.

Shen, C. Y. & Evans, T. E. 2002 Inertial instability and sea spirals. *Geophys. Res. Lett.* **29**, 2124.

Sipp, D. & Jacquin, L. 2000 Three-dimensional centrifugal-type instabilities of two-dimensional flows in rotating systems. *Phys. Fluids* **12**, 1740–1748.

Sipp, D., Fabre, D., Michelin, S. & Jacquin, L. 2005 Stability of a vortex with a heavy core. *J. Fluid Mech.* **526**, 67–76.

Stevens, D. E. 1983 On symmetric stability and instability of zonal mean flows near the equator. *J. Atmos. Sci.* **40**, 882–893.

Stevens, D. E. & Ciesielski, P. E. 1986 Inertial instability of horizontally sheared flow away from the equator. *J. Atmos. Sci.* **43**, 2845–2856.

Taniguchi, H. & Ishiwatari, M. 2006 Physical interpretation of unstable modes of a linear shear flow in shallow water on an equatorial beta-plane. *J. Fluid Mech.* **567**, 1–26.

Toloza, J. H. 2001 Exponentially accurate error estimates of quasiclassical eigenvalues. *J. Phys.* A **34**, 1203–1218.

Winter, T. & Schmitz, G. 1998 On divergent barotropic and inertial instability in zonal-mean flow profiles. *J. Atmos. Sci.* **55**, 758–776.

Yavneh, I., McWilliams, J. C. & Molemaker, M. J. 2001 Non-axisymmetric instability of centrifugally stable stratified Taylor–Couette flow. *J. Fluid Mech.* **448**, 1–21.

Young, W. R. & Ben Jelloul, M. 1997 Propagation of near-inertial oscillations through a geostrophic flow. *J. Mar. Res.* **55**, 735–766.